A NEW TECHNIQUE TO CHARACTERIZE FRACTURES IN TIGHT RESERVOIRS USING NEUTRON POROSITY LOGS ENHANCED BY ELECTRICALLY TRANSPORTED CONTRAST AGENTS

A Thesis

by

HEWEI TANG

Submitted to the Office of Graduate and Professional Studies of
Texas A&M University
in partial fulfillment of the requirements for the degree of

MASTER OF SCIENCE

Chair of Committee,	John E. Killough
Committee Members,	Maria A. Barrufet
	Zoya Heidari
Head of Department,	A. Daniel Hill

August 2016

Major Subject: Petroleum Engineering

Copyright 2016 Hewei Tang

ABSTRACT

In situ evaluation of fracture density has always been challenging for the petroleum industry, although it is required for a reliable reservoir characterization. Production can be directly controlled by induced and natural fracture density, especially in tight reservoirs. A previous publication introduced a method of using high thermal neutron capture cross-section contrast agents such as boron carbide to enhance the sensitivity of neutron logs to the presence of fractures. However, due to the transport limitations, all of the previous studies are focused on locating the proppants. The possibility of utilizing this method to characterize the fracture density in un-propped area has not yet been investigated. In this paper, we propose a new technique of applying electrical potential to enhance the transport of these contrast agents into induced and natural fractures. The boron carbide contrast agents, if well distributed in natural fractures, will enhance the sensitivity of nuclear logs (e.g., neutron porosity logs) to the presence and density of fractures.

To fulfill the aforementioned objectives, we numerically estimated electric field potential and simulated fluid flow in the fractured formations. The spatial distribution of contrast agents transported using the electrical field potential is then estimated by numerically solving the governing equations derived from electrophoretic velocity and material balance formulations. Furthermore, we simulated neutron porosity logs by solving neutron diffusion equations, which significantly reduces (from hours to few seconds) the computing cost compared to conventional use of MCNP (Monte Carlo N-Particle Code) technique.

The simulation results confirmed that an external electric field can significantly expedite the transport of charged contrast agents in the fracture network. Sensitivity analysis revealed that increasing particle zeta potential can efficiently decrease the transport time. Single fracture model was compared to previously published results obtained from MCNP, which confirmed the accuracy of the method and the effectiveness of baron carbide contrast agents in enhancing the neutron porosity logs. In the presence of 1wt% contrast agents, the minimum fracture width that can be directly detected is 0.01cm. This limit decreases, if the concentration of contrast agents increases. Furthermore, complex fracture models were presented with different secondary fracture density ranging from 1% to 8% and a single hydraulic fracture functioned as the source of the contrast agents. The relative change of simulated neutron porosity before and after applying electric potential field was calculated and compared at different transport time. The favorable detection time to quantify fracture density in the case was also determined. In conclusion, we demonstrated that the new technique enables the successful application of neutron porosity logs in fracture characterization including assessment of secondary fracture density, if combined with other logging tools.

ACKNOWLEDGEMENTS

I would like to sincerely thank my supervisor, Dr. John Killough, for inspiring me to pursue such an interesting research topic. Through his outstanding support and insight, I was able to explore the beauty of petroleum engineering, reservoir simulation and formation evaluation.

I would also like to express my gratitude to my committee member, Dr. Zoya Heidari. Her invaluable advice on my research made the development of this project more solid and convincible. I also want to take this opportunity to thank Dr. Maria Barrufet, for her time to review my work and give insightful comments.

Thanks also go to members in my research group, who gave me aids during my research. My deepest gratitude goes to Bicheng Yang, Cheng An, Jie He, Yang Cao, Masoud Alfi, and Dr. Mohamed Fadlelmula.

I would like to thank Chrisman Institute of Petroleum Department, Texas A&M University for financially supporting this project.

Finally, I would express my sincere gratitude to my parents for providing me the best education opportunities and to Zhuang for his love and support.

NOMENCLATURE

μ	Electrophoretic mobility, $\mathrm{m^2 s^{-1} V^{-1}}$
ε_w	Dielectric permittivity of dispersion medium, $\mathrm{Farads/m}$
μ_w	Dynamic viscosity of the dispersion medium, $\mathrm{Pa \cdot s}$
ξ	Zeta potential, V
a	Particle radius, m
κ	Debye length, m
Du	Dukhin number
σ	Electric conductivity, $\mathrm{S/m}$
R_w	Water resistivity, $\Omega \cdot \mathrm{m}$
R_r	Rock resistivity, $\Omega \cdot \mathrm{m}$
F	Formation resistivity factor
v	Electrophoretic velocity, $\mathrm{m/s}$
Ψ	Electrical potential, V
ε_0	Dielectric permittivity of free space, $\mathrm{Farads/m}$
ε_r	Dielectric constant
T	Temperature, ℃
m	Mass flux of particles, $\mathrm{kg/m^2}/s$
C	Concentration of particles, $\mathrm{kg/m^3}$
ϕ	Porosity
S_w	Saturation
t	Electrically transport time, s

x	Electrically transport distance, m
ξ	Particle zeta potential, mV
$\widetilde{m}$	Sink or source of the mass flux of particles, $\mathrm{kg/m^2}/s$
φ_1	Epithermal neutron flux, neutrons/cm^2/s
φ_2	Thermal neutron flux, neutrons/cm^2/s
Σ_{r_1}	Scattering cross section, 1/cm
Σ_{r_2}	Absorption cross section, 1/cm
D_1, D_2	Diffusion coefficient, cm
S	Source strength, neutrons/cm^3/s
L_s	Slowing down length, cm
L_d	Diffusion length, cm
L_m	Migration length, cm

TABLE OF CONTENTS

Page

ABSTRACT ii

ACKNOWLEDGEMENTS iv

NOMENCLATURE v

TABLE OF CONTENTS vii

LIST OF FIGURES ix

LIST OF TABLES xii

CHAPTER I INTRODUCTION 1

1.1 Problem Statement 1
1.2 Literature Review 1
1.3 Objectives and Approaches 4

CHAPTER II NUMERICAL SIMULATION METHODS 6

2.1 Introduction 6
2.2 Electrically Transport in Porous Media 6
2.3 Neutron Porosity Logs Simulation 10
2.4 Coupled Simulation of Electrically Transport and Neutron Porosity Logs 15

CHAPTER III ELECTRICALLY TRANSPORT SIMULATION RESULTS 17

3.1 Verification of Electrophoretic Velocity Equation 17
3.2 1D Analytical/Numerical Solutions and Sensitivity Analysis 18
3.3 2D Case and Analysis of Particles Leakage into the Matrix 22

CHAPTER IV NEUTRON POROSITY LOGS SIMULATION RESULTS 27

4.1 Verification with MCNP Code 27
4.2 Single Fracture Sensitivity Analysis.....29
4.3 Multi Fractures Characterization 35

CHAPTER V SYNTHETIC CASES FOR FRACTURE CHARACTERIZATION 38

5.1 Introduction 38
5.2 Evenly Spaced Fractures Characterization 38
5.3 Formations with Different Secondary Fracture Densities 41

CHAPTER VI CONCLUSIONS 54

REFERENCES.....57

LIST OF FIGURES

Page

Figure 1. Schematic diagram of the 1D mass balance of particle flow.....8

Figure 2. Slowing-down lengths for AmBe source neutrons to reach 0.4eV for limestone, sandstone and dolomite formation (reprinted from Ellis,D.V, et al., 1987).. 14

Figure 3. Migration length as a function of formation porosity for the three principal lithologies (reprinted from Ellis,D.V, et al., 1987) 14

Figure 4. Comparison of experimental electrophoretic velocity (v-exp, Fang et al., 1991) and simulated electrophoretic velocity (v-sim) at different temperature for different electric field strength (156.9V/m and 261V/m). 18

Figure 5. Particle flow concentration distribution via time (the scale is in kg/m^3).....21

Figure 6. Particle concentration via transport distance for different transport time and electric field strength (particle zeta potential = 100mv).....21

Figure 7. Particle concentration via transport distance for different transport time and particle zeta potential (electric field strength =150V/m).....22

Figure 8. Synthetic formation (a) and electric field distribution (b) 23

Figure 9. Particle spatial distribution after (a)2h, (b)4h, (c)6h, (d)8h transport for matrix porosity=0.03 24

Figure 10. Particle spatial distribution after (a)2h, (b)4h, (c)6h, (d)8h transport for matrix porosity=0.1 25

Figure 11. Particle spatial distribution after (a)2h, (b)4h, (c)6h, (d)8h transport for matrix porosity=0.15 26

Figure 12. Simulation results comparison of MCNP code (Duenckel et al. 2012) and neutron diffusion equation.....28

Figure 13. Schematic diagram of Neutron Porosity Log simulation.....30

Figure 14. Neutron count rate for different contrast agents concentration (fracture width=0.2cm).....30

Figure 15. Neutron count rate for different fracture width (contrast agents concentration = 0.2g/cm3). 31

Figure 16. Maximum neutron count rate decrease for different fracture width (contrast agents concentration = 0.2g/cm3) 32

Figure 17. The impact of formation porosity on Neutron Porosity Logs (matrix capture cross section equals to 10 c.u.). 33

Figure 18. The impact of different matrix capture cross section on Neutron Porosity Logs (matrix porosity =0.1). 34

Figure 19. Neutron Porosity Logs for different formation lithology. 35

Figure 20. Schematic Diagram of two parallel fractures simulation. 36

Figure 21. Neutron Porosity Logs for different fracture distance (2cm-6cm). 37

Figure 22. Neutron Porosity Logs for different fracture distance (8cm-16cm). 37

Figure 23. Synthetic formation with evenly spaced fractures: particles spatial distribution after applying electric field for (a) 2h, (b) 4h, (c) 8h. 40

Figure 24. Synthetic formation with evenly spaced fractures: neutron porosity logs after applying electric field for (a) 2h, (b) 4h, (c) 8h. 40

Figure 25. Synthetic formation with different natural/induced fracture density of 1%, 2%, 4% and 8%. 41

Figure 26. Electric field distribution of the synthetic formation. 42

Figure 27. Particle spatial distribution after applying electric field for 2h, 4h, and 6h. Formations with fracture density of 1%, 2%, 4% and 8% are compared (matrix porosity = 0.03, the concentration is in kg/m^3). 44

Figure 28. Neutron Porosity Logs after applying electric field for (a) 2h, (b) 4h, and (c) 6h, formations with different fracture densities are compared (matrix porosity = 0.03). 46

Figure 29. Relative change of Φ_N before and after applying electric field for (a) 2h, (b) 4h, and (c) 6h, formations with different fracture densities are compared (matrix porosity = 0.03). 47

Figure 30. Total particle concentration in formation via transport time for formations with different fracture density 49

Figure 31. Particle spatial distribution after applying electric field for 2h, 4h, and 6h. Formations with fracture density of 1%, 2%, 4% and 8% are compared (matrix porosity = 0.1, the concentration is in kg/m3). 50

Figure 32. Neutron Porosity Logs after applying electric field for (a) 2h, (b) 4h, and (c) 6h, formations with different fracture densities are compared (matrix porosity = 0.1). 51

Figure 33. Relative change of Φ_N before and after applying electric field for (a) 2h, (b) 4h, and (c) 6h, formations with different fracture densities are compared (matrix porosity = 0.1) 52

LIST OF TABLES

Page

Table 1. Coefficient of Eq. (29) to evaluating Ls. 13

Table 2. Coefficient of Eq. (29) to evaluating D_2. 13

Table 3. Properties of the synthetic formations and fractures 23

Table 4. Macro-parameters for a sandstone formation with a porosity of 0.283 in neutron diffusion equation 29

Table 5. Average difference and error between MCNP5 simulation results and neutron diffusion equation simulation results for different fracture width. 29

Table 6. Maximum neutron count rate decrease in the detector, for different fracture spacing formations and for different transport time. 39

CHAPTER I

INTRODUCTION

1.1 Problem Statement

Hydraulic fracturing is of high importance in current oil and gas production activities, especially for reservoirs with low porosity and low permeability. Hydraulically-induced fractures improve the well productivity by dramatically increasing the well-reservoir contact area. Sharma and Manchanda (2015) proved the presence of induced un-propped fractures and their important role in the productivity of hydraulically fractured wells. To distinguish from hydraulic fractures, induced fractures together with natural fractures are often referred to as secondary fractures. Characterization of secondary fractures is particularly difficult because they are much smaller than major hydraulic fractures in size (usually in millimeters) (Dahi et al., 2013). In this research project, we will approach this problem by proposing a new secondary fracture characterization technique by combining the electrically transported contrast agents and neutron porosity logs.

1.2 Literature Review

The currently existing fracture characterization techniques can be roughly divided into two categories: far-field and near wellbore techniques (Saldungaray et al., 2012). Tilt meters and microseismic tools are two representatives of far-field techniques that have been used for years. The principle of tilt meter fracture mapping is to infer fracture geometry by measuring the fracture-induced rock deformation, which can either be

measured with a surface array of tiltmeters or with downhole titltmeters arrays (Wright et al.,1998). Microseismic tools have also been used to map hydraulic fracture stimulations of reservoirs. New fractures are mapped and calibrated during fracturing operations by monitoring subsurface microseismic activities (Hunt et al., 2010). However, both tools only provide a rough picture of fracture dimension without a satisfying resolution for the presence of secondary fractures.

For near wellbore techniques, borehole image logging tools and sonic logs are commonly used in detecting fractures. However, the presence of secondary fractures will sometimes be hardly recognized due to their tiny width. Chi et al. (2014) proposed a method of combined interpreting NMR and Electromagnetic logs to assess micro-fracture density. They tested the method on pore-scale carbonate images and organic shale images with artificial micro-fractures. However, the proposed method is not applicable to case-hole environment. Martinez et al. (2002) applied fuzzy inference systems to integrate different well logs to identify the presence of fractures. They concluded that no single conventional well logging tool can provide a reliable characterization of fractures in the wellbore.

Nuclear logging tools, which are applicable for both open-hole and case-hole environment, raised researchers' interest. Radioactive tracers were mixed with fracturing fluid and detected by gamma ray detectors after fracturing to locate the fracture interval (Gadekea et al., 1991). Due to the environmental concerns of using radioactive materials, Mulkern et al. (2010) introduced field applications of utilizing boron carbide (CB_4) tagged proppants to locate proppants and determine fracture height. Boron carbide is a high

thermal neutron capture cross section material, which will dramatically decrease the number of thermal neutrons counted by the neutron logging tools. Later, Duenckel et al. (2012) validated the feasibility of this method with the Monte Carlo N-Particle Transport Code (MCNP). However, due to the transport limitation, none of the previous researchers have explored the possibility of utilizing this method to characterize fracture density in un-propped areas.

In this work, an external electric field was applied to enhance the transport of charged boron carbide particles into the secondary fracture network. The introduction of an external electric field in field operation is not a difficult task since the external electric field is commonly applied in electric resistivity log and electrical enhanced oil recovery process. However, to our limited knowledge, the direct study of charged particles transport under electric field in subsurface porous media is still limited in the oil and gas industry.

Electrophoretic movement of particles is a reflection of balanced electrical, hydrodynamic and steric interaction forces (Hill, 2007). According to Henry (1948), the electrophoretic velocity of an insulating spherical particle is related to its radius, zeta potential, electrical conductivity and viscosity of transport media. Particle surface in contact with aqueous media is more often negatively charged because of the absorption of less hydrated anions (Huotari et al., 1999). This is a good news for subsurface application because downhole clays are usually considered to be negatively charged, and thus the particles will be hardly absorbed by the formation. In this paper, we will combine the electrophoretic model proposed by Smoluchowski (1924) and a material balance analysis

of particle flow in porous media to derive a governing equation for the electrically transported particles.

1.3 Objectives and Approaches

The objectives of this paper include (a) quantifying the impact of electric field strength and contrast agents' zeta potential on the transport time and distance of the contrast agents, (b) quantifying the sensitivity of neutron porosity logs to fracture properties (width and length) in the presence of the contrast agents in the fractured zones, and (c) quantifying the spatial distribution of contrast agents in the near wellbore region of the synthetic fractured formation under the electric field and the impact of the contrast agents' spatial distribution on the neutron porosity logs.

To fulfill the aforementioned objectives, the whole process was numerically simulated:

(1) Simulation of electrical enhanced particle transport

The electric field potential is estimated by the Laplace conductivity equation. Upon the solved electric potential field, the particle spatial distribution can be obtained by solving the governing equation derived from electrophoretic velocity and material balanced formulations.

(2) Simulation of Neutron Porosity Logs

The neutron porosity log signal is simulated by solving neutron diffusion equations. Comparison of the results obtained from solving diffusion equations against those from MCNP (Monte Carlo N-Particle Code) confirmed the accuracy of this simplified method for the examples documented in this research. Meanwhile, this simplified and fast forward

simulation of neutron logs significantly reduced (from a few hours to a few seconds) the computing cost.

(3) Combination of the two parts of simulation

The most important parameter influencing the thermal neutron count rate in the neutron diffusion equation, macroscopic cross section, is proportional to the microscopic and molecular density of each isotope. Thus, the parameters in the equation can be correlated to the concentration of boron carbide.

CHAPTER II

NUMERICAL SIMULATION METHODS

2.1 Introduction

To improve the in situ evaluation of secondary fractures, we proposed to inject charged boron carbide particles with hydraulic slurry, electrically distribute them into secondary fractures, and record neutron porosity measurements before and after applying the electrical potential. Numerical simulations of the procedure were conducted to investigate the feasibility of the technique. A physical model derived from electrophoretic velocity and material balance formulations was proposed and solved to simulate the spatial distribution of contrast agents. Furthermore, we simulated neutron porosity logs by solving neutron diffusion equations, which significantly reduced (from hours to a few seconds) the computing cost compared to conventional use of MCNP (Monte Carlo N-Particle Code) technique. Finally, the simulation of electrically transport and Neutron Porosity Log were combined to characterize fractured formation, through the spatial distribution of contrast agents. A more detailed description is described in the following sections.

2.2 Electrically Transport in Porous Media

Electrophoresis process describing the migration of charged colloidal particles under the influence of an electric field. In 1948, Henry proposed a general electrophoretic mobility model of insulating and rigid spherical particles based on the classical model of Smoluchowski (1924) :

$$\mu = \frac{2\varepsilon_w}{3\mu_w}\{1 + 2\lambda[f(\kappa a) - 1]\}\xi \tag{1}$$

In the equation, μ is the electrophoretic mobility (in $\mathrm{m^2 s^{-1} V^{-1}}$) ε_w is the dielectric permittivity of dispersion medium (in $\mathrm{Farads/m}$), μ_w is the dynamic viscosity of the dispersion medium (in $\mathrm{Pa \cdot s}$), ξ is zeta potential (in V), a is particle radius (in m), κ is a Debye length.

$$\lambda = \frac{1 - 2Du}{2 + 2Du} \tag{2}$$

Du is the "Dukhin number",

$$Du = \frac{\sigma_s}{2\sigma_w} \tag{3}$$

Where σ_s and σ_w are the electric conductivity of surface and water.

$f(\kappa a)$ is a correction factor considering retardation effect, whose value ranges from 0.5 to 1.5 (Leroy et al. 2011). When the term $\{1 + 2\lambda[f(\kappa a) - 1]\}$ equals to 1.5, the equation will reduce to the traditional Smoluchowski theory, which is general suitable for large non-conducting particles ($\kappa a \gg 1$). When the term $\{1 + 2\lambda[f(\kappa a) - 1]\}$ equals to 1, the equation will reduce to the Huckel theory, which is general suitable for nanoparticles, where Debye length is larger than particle radius ($\kappa a < 1$).

Since we need the contrast agent particles to transport into induced and natural fractures, whose width is general considered to be in micro scale, a classical Smoluchowski equation will best fit our purpose. Thus, the electrophoretic velocity will be expressed as:

$$v = -\frac{\varepsilon_w \xi}{\mu_w}\nabla\Psi \tag{4}$$

In the equation, v is the electrophoretic velocity (in ms^{-1}), Ψ is the electrical potential (in V). We assume the dispersion media to be water. The dielectric permittivity of water can be calculated by:

$$\varepsilon_w = \varepsilon_r \varepsilon_0 \tag{5}$$

$\varepsilon_0 = 8.85 \times 10^{-12} \quad Farads/m$ is the permittivity of free space and ε_r is the dielectric constant of water, which can be correlated with temperature (°C) by the following equation (Trusdell and Jones, 1973):

$$\varepsilon_r = 87.74 + (-0.4008 + (9.398 \times 10^{-4})T - (1.41 \times 10^{-6})T^2) \times T \tag{6}$$

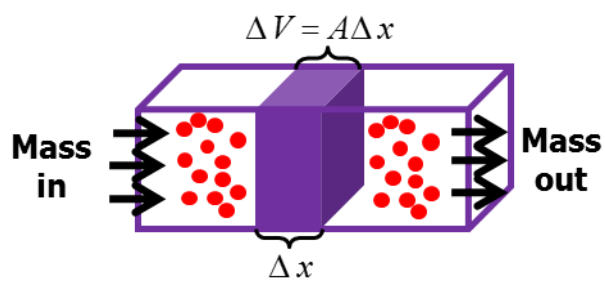

Figure 1. Schematic diagram of the 1D mass balance of particle flow

Assuming the particle flow is continuous, the mass balance of particle flux in a formation of porosity ϕ and saturation S_w can be expressed as follows (Fig.1 provides a schematic diagram of the mass balance of particle flow):

$$m_x A\Delta t - m_{x+\Delta x} A\Delta t + \tilde{m}\Delta V \Delta t = \Delta V \phi S_w C_{t+\Delta t} - \Delta V \phi S_w C_t \tag{7}$$

It can be reduced to:

$$\frac{m_x - m_{x+\Delta x}}{\Delta x} + \tilde{m} = \frac{\phi S_w C_{t+\Delta t} - \phi S_w C_t}{\Delta t}, \tag{8}$$

where m_x is the mass flux of particle flow, which is defined as the following:

$$m_x = Cu_x, \tag{9}$$

where C is the concentration of particles, and u_x is the electrophoretic velocity of particle flow. Incorporating Equation (4) and (5) into the Equation (8), and letting$\Delta x \to 0,\ \Delta t \to 0$, we can obtain the following formula:

$$\frac{\partial}{\partial x}\left(C\frac{\varepsilon_r\varepsilon_0\xi}{\mu_w}\frac{d\Psi}{dx}\right) = \frac{\partial(\phi S_w C)}{\partial t} - \widetilde{m}, \tag{10}$$

where $\widetilde{m}$ is the sink and source term in the equation. All the terms in the equation is in SI units. According to S Lee (1990) , an additional term is added to Equation (10) to account for the tortuosity of porous media.

$$\frac{\partial}{\partial x}\left(C\frac{\varepsilon_r\varepsilon_0\xi}{\mu_w}\frac{\phi}{\Gamma}\frac{d\Psi}{dx}\right) = \frac{\partial(\phi S_w C)}{\partial t} - \widetilde{m} \tag{11}$$

$$\Gamma = \frac{1}{\phi^n} \tag{12}$$

In the simulation, n is set to be 2 for the low porosity formation. Equation (11) is the final governing equation of the electrically-transported particle flow in porous media. Equations for other directions can be derived in the same way.

To solve Equation (11), we need to first estimate the electric field through the following Laplace Equation:

$$\nabla \cdot (\sigma \cdot \nabla\Psi) = 0\,, \tag{13}$$

where, σ is the electric conductivity in S/m. The equation can be solved by finite different method with a constant electric potential difference being set for the two boundaries in the interested direction.

With electric field calculated, Equation (11) can be solved by the following discretizing formula:

$$T_{i+}E_{i+}C_i[flag(i+)] + T_{i+}E_{i+}C_{i+1}[\sim flag(i+)] - T_{i-}E_{i-}C_i[\sim flag(i-)]$$

$$- T_{i-}E_{i-}C_{i-1}[flag(i-)] = \frac{\phi_i S_{wi} V_i}{\Delta t}(C_i^{n+1} - C_i^n), \tag{14}$$

where,

$$T_{i+} = \frac{h_{i+}}{(\Delta x_+)^2} \tag{15}$$

$$h_{i+} = \frac{2h_i h_{i+1}}{h_i h_{i+1}} \tag{16}$$

$$h_i = \frac{\varepsilon_r \varepsilon_0 \xi}{\mu_w} \frac{\phi_i}{\Gamma_i} \tag{17}$$

$$E_{i+} = \frac{\Psi_{\mathrm{i+1}} - \Psi_{\mathrm{i}}}{\Delta x_+} \tag{18}$$

$$E_{i-} = \frac{\Psi_{\mathrm{i}} - \Psi_{\mathrm{i-1}}}{\Delta x_-} \tag{19}$$

$$flag(i+) = (\Psi_{\mathrm{i}} > \Psi_{\mathrm{i+1}}), \qquad logical\ variable \tag{20}$$

$$flag(i-) = (\Psi_{\mathrm{i-1}} > \Psi_{\mathrm{i}}), \qquad logical\ variable \tag{21}$$

2.3 Neutron Porosity Logs Simulation

Based on the broad ranges of energy, neutrons are usually categorized in three groups: fast neutrons (energy in MeV region), epithermal neutrons (energy in the range of 0.4eV to several eV) and thermal neutrons (in thermal equilibrium with the surrounding medium). The common used neutron logging source, Americium-Beryllium (AmBe) source generates neutrons with average energy about 4.2 MeV, which lies in the range of

epithermal neutrons. After released into formation, the source neutrons will mainly participate in two kinds of interactions: elastic scattering and thermal absorption. The energy loss during the first process, elastic scattering, mainly depends on the mass of the target isotope struck by the neutron and the scattering angle. Among various isotopes, hydrogen is the most efficient one in reducing the colliding neutron energy. All source neutrons will eventually be in thermal equilibrium if they are not absorbed by absorbers. The latter is the thermal absorption process, which terminates the life of a neutron, and depress the thermal neutron flux a lot. We are interested in these thermal neutrons because the detector are most sensitive to them.

A formal description of neutron transport is given by the Boltzmann Transport Equation as shown in Equation (22). It is an accurate physical model, which is commonly solved by Monte Carlo N-Particle Code (MCNP). The method is physically sound but computationally inefficient, and the usual computational time is in hours.

$$\frac{1}{v}\frac{\partial\psi}{\partial t} + \Omega \cdot \nabla\psi + \Sigma_t\psi = \frac{\chi_p}{4\pi}\int dE\nu_p\Sigma_f\phi + \sum\frac{\chi_{di}}{4\pi}\lambda_i C_i + \int d\Omega\int dE'\Sigma_s\psi + s \qquad (22)$$

The equation can be simplified by grouping the neutrons into two energy groups, epithermal and thermal neutron flux, and assuming that the angular flux is only weakly dependent on the direction:

$$D_1\nabla^2\varphi_1 - \Sigma_{r_1}\,\varphi_1 + S = 0$$

$$D_2\nabla^2\varphi_2 - \Sigma_{r_2}\,\varphi_2 + \Sigma_{r_1}\,\varphi_1 = 0 \qquad (23)$$

The equations are called neutron diffusion equations, which were proposed by Allen et al. in 1967. In the equations, φ_1 is epithermal neutron flux, and φ_2 is thermal neutron flux

(in neutrons/cm^2/s). Σ_{r_1} is the scattering cross section , and Σ_{r_2} is the absorption cross section (in 1/cm). D_1 and D_2 are diffusion coefficient (in cm). S is the source strength (in neutrons/cm^3/s). The equation can be solved in seconds by finite difference method. The parameters are correlated as follows:

$$L_s = \sqrt{D_1/\Sigma_{r_1}} \tag{24}$$

$$L_d = \sqrt{D_2/\Sigma_{r_2}} \tag{25}$$

$$L_m^2 = {L_s}^2 + {L_d}^2 \tag{26}$$

$$D_2 = \frac{1}{3(\Sigma_{r_1}+\Sigma_{r_2} - \mu\Sigma_{r_1})} \tag{27}$$

$$\mu = \frac{2}{\pi} = 0.637 \tag{28}$$

L_s is the slowing down length (in cm), L_d is the diffusion length (in cm), L_m is the migration length in cm. According to Ellis, et al. (1987), both L_s and D_2 can be evaluated by the following formula:

$$L_s \; or \; D_2 = c_1(\phi + c_3)^{c_2} + c_4 \tag{29}$$

The values of the four constants for the three typical lithology are shown in Table 1. and Table 2. The parameters via different porosity can also be gained by referring to Fig.2 and Fig.3. Based on these two figures, there are no significant difference of Neutron Diffusion Parameters for these three lithology at a single porosity.

Table 1.Coefficient of Eq. (29) to evaluating Ls.

	Limestone	Sandstone	Dolomite
c_1	3.762	5.953	2.699
c_2	-0.5145	-0.3972	-0.5948
c_3	0.0379	0.0223	0.0545
c_4	4.141	1.940	5.475

Table 2. Coefficient of Eq. (29) to evaluating D_2.

	Limestone	Sandstone	Dolomite
c_1	0.1933	0.1874	0.1962
c_2	-0.9950	-1.003	-1.003
c_3	0.1366	0.1107	0.1627
c_4	-0.0011	0.0006	0.0005

L_s and L_m can also be evaluated from Fig.2 and Fig.3 (Ellis et al., 2007) .

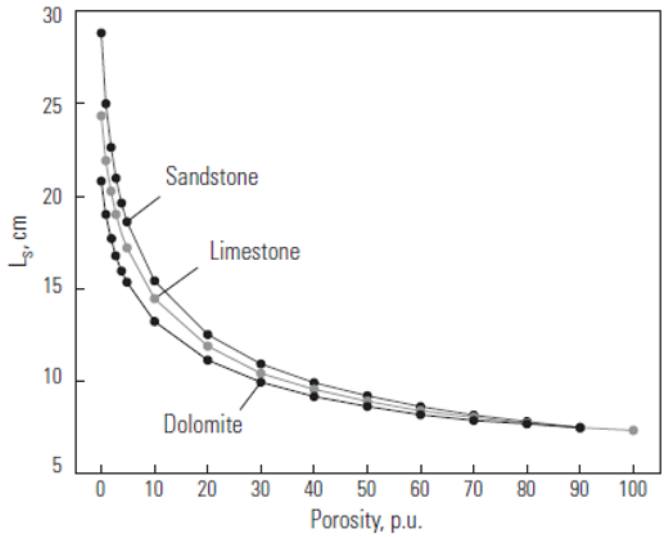

Figure 2. Slowing-down lengths for AmBe source neutrons to reach 0.4eV for limestone, sandstone and dolomite formation (reprinted from Ellis,D.V, et al., 1987).

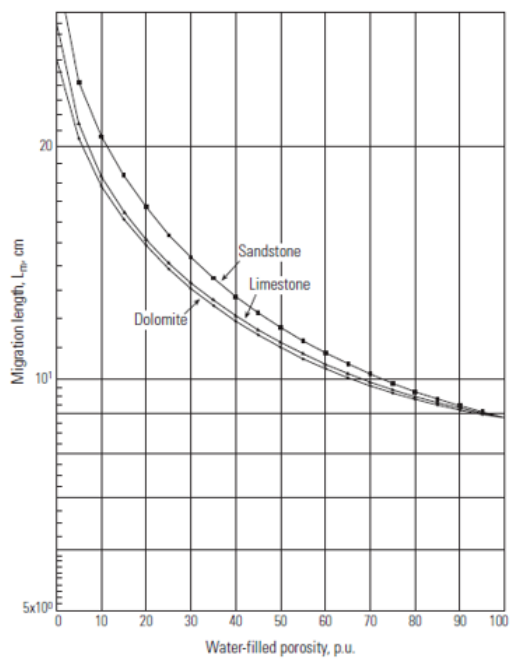

Figure 3. Migration length as a function of formation porosity for the three principal lithologies (reprinted from Ellis,D.V, et al., 1987).

2.4 Coupled Simulation of Electrically Transport and Neutron Porosity Logs

The top neutron absorbing element is Boron. Boron Carbide (CB_4), a ceramic compound with 75% of Boron by weight, has been patented for tracing the hydraulic fracturing proppants (Duenckel et al., 2012). In this work, we proposed to mix proppants with Boron Carbide particles, electrically distribute them into secondary fractures, and assess the neutron logs before and after applying the electric field. Because of the detection depth limitation (usually about 20cm) of neutron logging tool, we are only able to assess the near wellbore unpropped area. In this case, the electrical field can be applied right after starting the fracturing job. Because at this time, the near well bore area has already been fractured and the electric field can further expedite the contrast agents from hydraulic fractures to induced and natural fractures. To simulate the whole procedure, we need to combine the two simulation techniques introduced above into a single simulator. The bridge between them is the spatial distribution of boron carbide particles and its influence on the macroscopic parameters in Neutron Diffusion Equations.

Among all the four parameters, neutron absorption cross section is the one that most influenced by neutron absorbers. The absorption cross section in the equation is the macroscopic cross section, which can be correlated with microscopic cross section by the following equation:

$$\Sigma = \sigma \frac{N_0}{A} \rho = \sigma_m \rho, \tag{30}$$

where, σ is the microscopic cross section, , N_0 is Avogadro's number, A is the atomic weight of the isotope, ρ is the density, σ_m is the mass-normalized absorption cross section. According to Ellis et al. (2007), the mass-normalized absorption cross section of Boron is

42.3 (cm^2/g). Thus, the macroscopic absorption cross section of fracture with boron carbide inside (CB_4) is:

$$\Sigma_{r_2} = C \times \phi \times Sw \times 42.3 \ \times 75\% = 32C\phi Sw \tag{31}$$

C is boron carbide concentration in (g/cm^3), which can be obtained from the simulation results of electrically transport. ϕ and Sw are the porosity and water saturation of fractures. In the simulation, we assume the porosity and water saturation of natural and induced fractures to be 1 and 0.4, while that of hydraulic fractures to be 0.6 and 1.

CHAPTER III

ELECTRICALLY TRANSPORT SIMULATION RESULTS

3.1 Verification of Electrophoretic Velocity Equation

The electrophoretic velocity calculated from equation (4)-(6) was compared with experimental results published by Fang et al. (1991). In the experiment, emulsified crude oil droplets were separated from water in an electrophoresis cell. The size of droplets was in a range of 1μm to 30μm, which just matches our expectation for the size of contrast agents. The zeta potential of droplets varied from 35mV to 60mV. The electrophoretic velocity was measured by reading the distance that oil droplet traveled in a given time. The experimental results of average electrophoretic velocity and the simulation results were compared in Fig.4. at different temperature for electric field strength of 156.9V/m and 261V/m respectively. The electrophoretic velocity in each case was normalized to the situation that particle zeta potential equals to 50mV for easy comparison (the zeta potential of oil droplets is in the range of 30 to 60 mV). The results confirmed the validation of using Smoluchowski equation to describe the electrophoretic velocity of contrast agents.

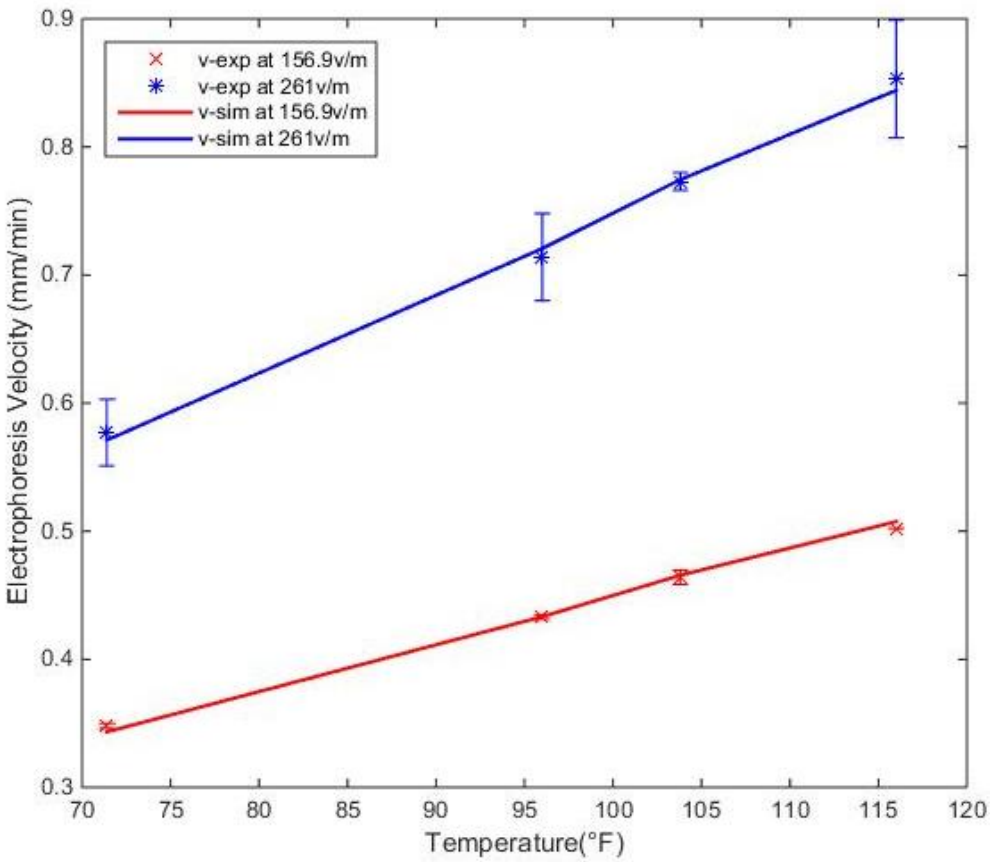

Figure 4. Comparison of experimental electrophoretic velocity (v-exp, Fang et al., 1991) and simulated electrophoretic velocity (v-sim) at different temperature for different electric field strength (156.9V/m and 261V/m).

3.2 1D Analytical/Numerical Solutions and Sensitivity Analysis

Assuming that particles, fluid and rock properties do not change via space and time, and assuming that there is no source term, then 1D transport governing equation (11) can be reduced to equation (32) under a constant electric field E.

$$\left(\frac{\varepsilon_r \varepsilon_0 \xi E}{\mu_w \Gamma S_w}\right)\frac{\partial C}{\partial x} = \frac{\partial C}{\partial t} \tag{32}$$

The general solution of this first order partial differential equation is:

$$C(x,t) = F\left(x + \frac{\varepsilon_r \varepsilon_0 \xi E}{\mu_w \Gamma S_w} t\right) \tag{33}$$

F(x) = C(x, 0) is the initial distribution of particles. If we set the boundary condition to be constant:

$$C(x,0) = 0\ (x > 0\ ) \tag{34}$$

$$C(0,t) = C_0 = 1\frac{kg}{m^3} \tag{35}$$

The concentration front will no longer be a sharp vertical line as it propagates. As a simplification, we take the location of $C_0/2$ as the location of concentration front. . Fig.5 shows the transport distance of concentration front with time for both numerical and analytical methods, which confirms the reliability of numerical solutions. For the case that, $\Gamma = 1$ and $S_w = 1$, the particles can be considered transporting in a free media, and the velocity will be just as same as the electrophoretic velocity of particles.

For the numerical simulation, we assumed that we have a 1m fracture in the core with a constant electrical potential difference of 150V applied at the two boundaries of it. The fracture was assumed to have a porosity of 1 and a constant saturation of 0.4. According to Plegue et al. (1986), crude oil-in-water emulsions (with a size in micro scale) have a range of zeta potential from 10 to 200mV, based on different pH and temperature values. It is reasonable to assume that the zeta potential of boron carbide particles, whose size is also in micro scale, will fall into this range. Thus, in the following cases, zeta potential of particles was commonly set as 100mV. And the fluid temperature was set as 40℃, remaining constant. The boundary condition was that at the high electrical potential

boundary, the particle fluid concentration was 1kg/m^3. And other parts of the fracture was initially free of particles.

The particle flow concentration distribution via different transport time was shown in Fig.5. Basically 10h was needed for particle flow with a zeta potential of 100mV to expedite a 1m fracture under a 150V/m electric field. To decrease the transport time, there are two parameters we can design: one is electric field strength and the other is the particle's zeta potential. The impact of electric field strength and particles zeta potential on the transport time and distance of particle flow are shown in Fig.6 and Fig.7 respectively. Increasing the electric field strength and particles zeta potential can both decrease the transport time needed for a specific transport distance. Comparing the two figures, we can conclude that increasing particles zeta potential has a more significant effect on accelerating the transport than increasing electric field strength. In addition, a higher zeta potential is always good for the stable existence of micro-scale or nano-scale particles.

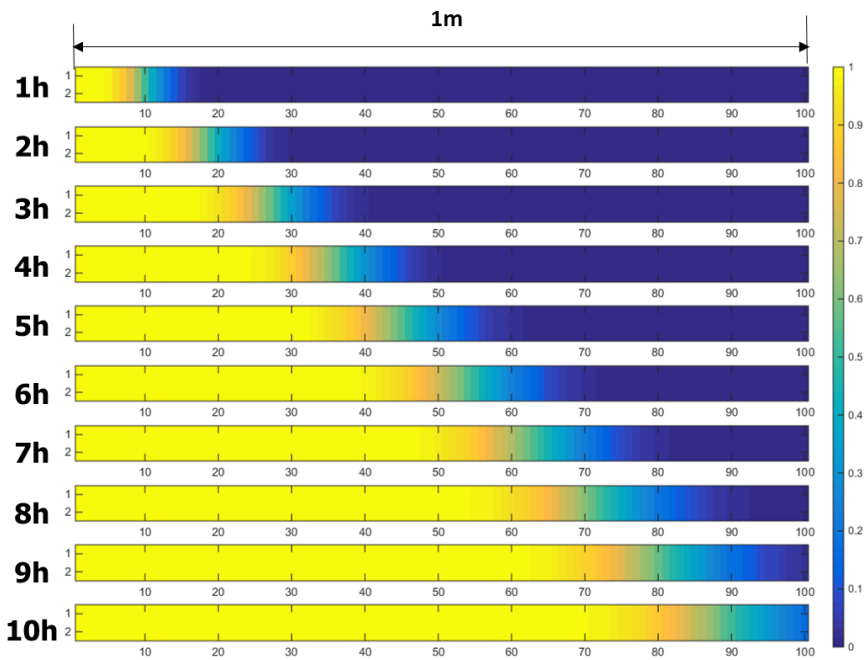

Figure 5. Particle flow concentration distribution via time (the scale is in kg/m^3)

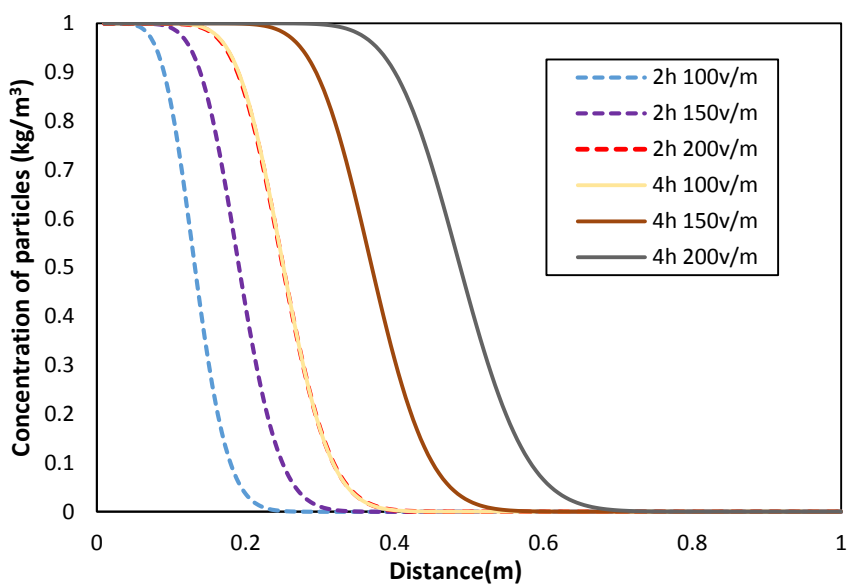

Figure 6. Particle concentration via transport distance for different transport time and electric field strength (particle zeta potential = 100mv).

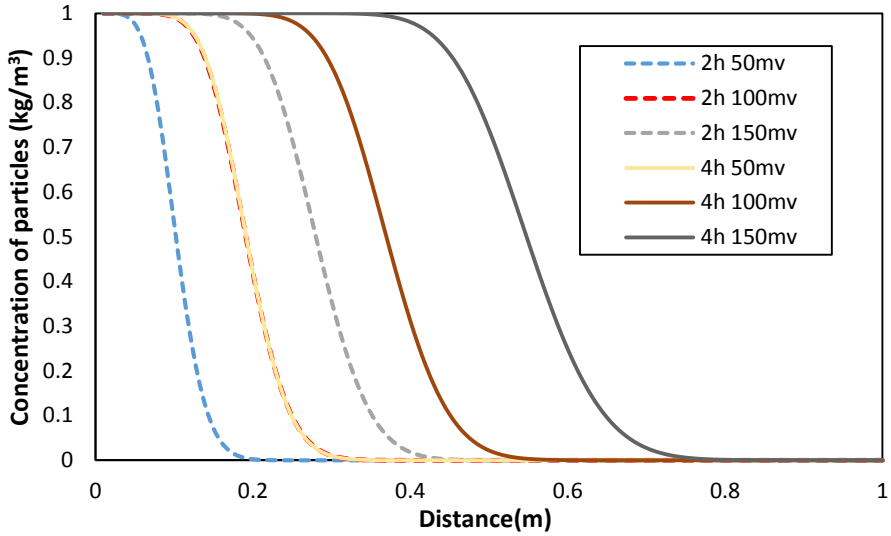

Figure 7. Particle concentration via transport distance for different transport time and particle zeta potential (electric field strength =150V/m)

3.3 2D Case and Analysis of Particles Leakage into the Matrix

According to Randolph et al.(1984) and Luffel et al.(1988), the porosity of tight gas sand reservoir usually falls into the range of 0.03 to 0.15. The porosity is usually the total porosity including the effect of natural fractures (An et al., 2016). So if we consider matrix and natural fractures as two separate media, the porosity of matrix will be even lower. In the following case, different matrix porosity is assigned to investigate the particles leakage into the matrix. As shown in Fig.8(a), A $20cm \times 20cm$ formation is assumed to have a hydraulic fracture functioned as the source of the particles, and with a constant particle concentration of 200kg/m^3 (0.2g/cm^3). Blue fractures represent natural and induced fractures. An electric potential of 30 V is applied to the perforation point A, and generate an electric field as shown in Fig.8(b). The generated electric field has an electric field strength of approximate 150V/m in x and y direction. Other properties of the

synthetic formation are shown in Table.3. The particle zeta potential is assumed to be 100mV.

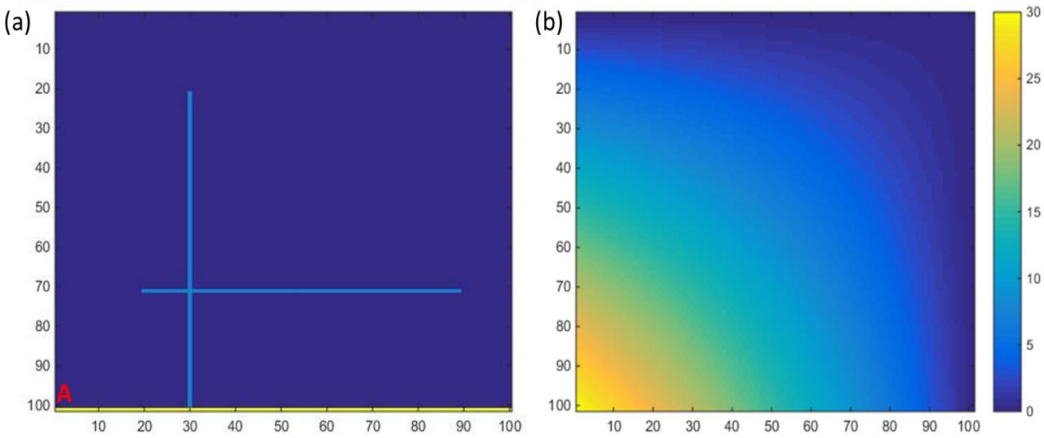

Figure 8. Synthetic formation (a) and electric field distribution (b)

Table 3. Properties of the synthetic formations and fractures

Parameter	**Value**	**Units**
Temperature	40	℃
Fluid viscosity	0.65×10^{-3}	$\mathrm{Pa \cdot s}$
Porosity of hydraulic fracture	0.6	-
Sw of hydraulic fractures	1	-
Sw of secondary fractures	0.4	-
Porosity of natural and induced fracture	1	-
Porosity of matrix	0.03, 0.1, 0.15	-
Sw of matrix	0.2	-
Connate water resistivity (R_w)	0.034	$\Omega \cdot \mathrm{m}$

The spatial distribution of particles via time for different matrix porosity formation is shown in Fig.9 to Fig.11. We can conclude from the simulation results that particles will not have significant leakage into the formation if the matrix porosity is less than 0.1. For the matrix porosity equaling to 0.15 case, the particles leakage into the formation is too significant that it cannot be ignored.

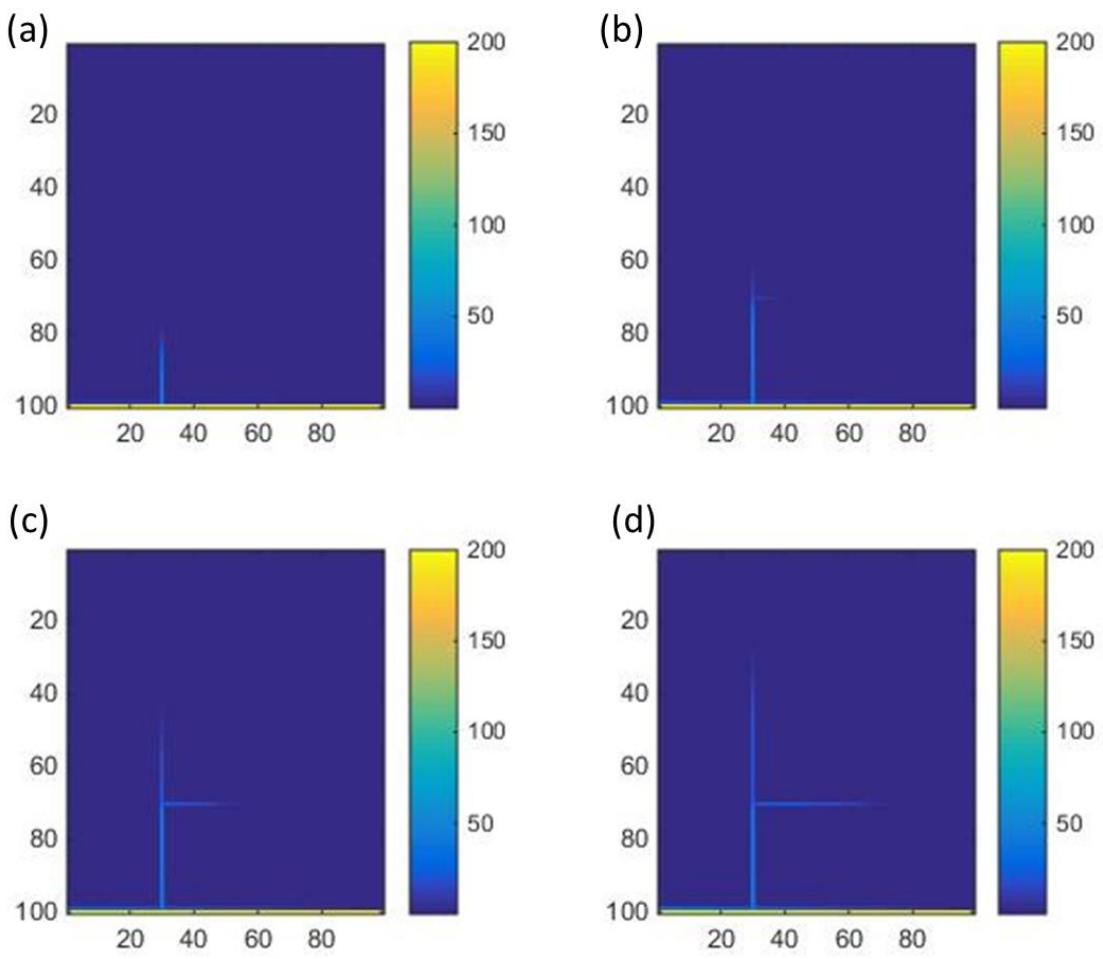

Figure 9. Particle spatial distribution after (a)2h, (b)4h, (c)6h, (d)8h transport for matrix porosity=0.03

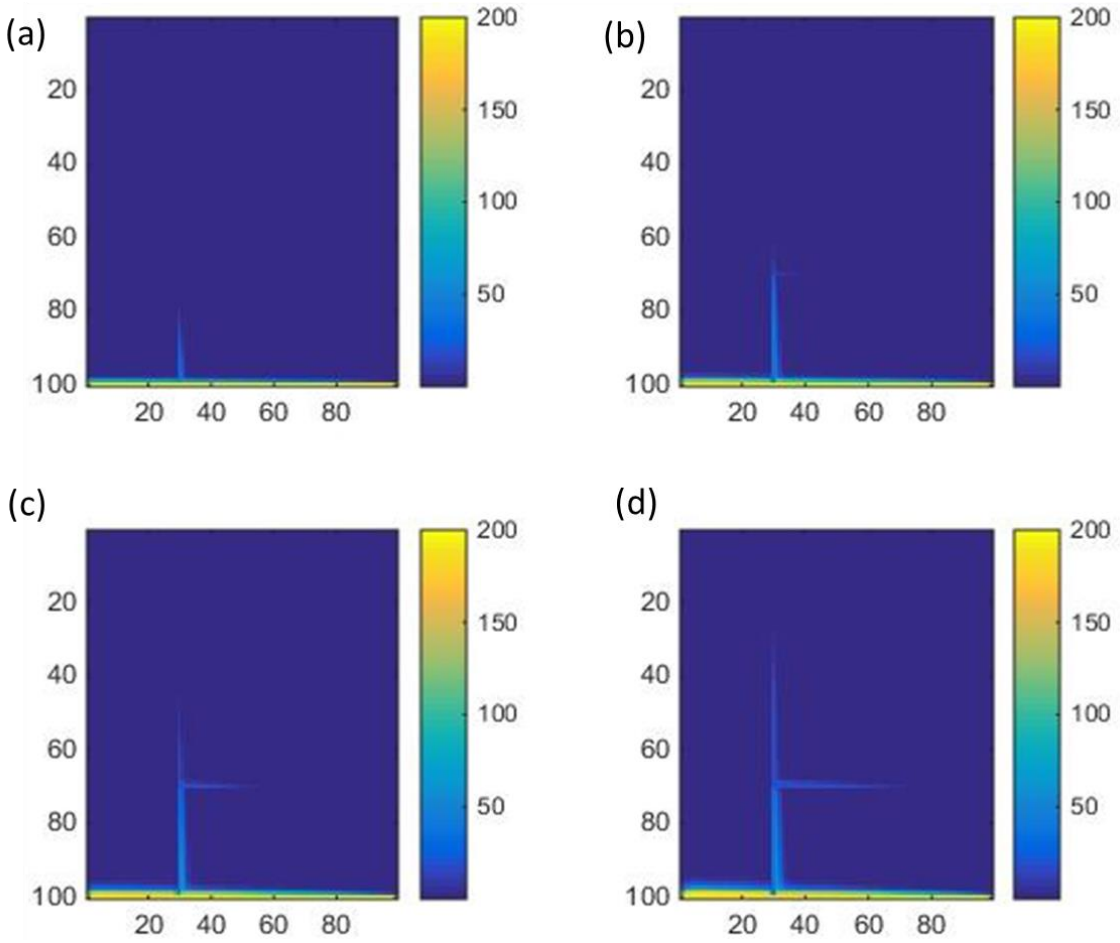

Figure 10. Particle spatial distribution after (a)2h, (b)4h, (c)6h, (d)8h transport for matrix porosity=0.1

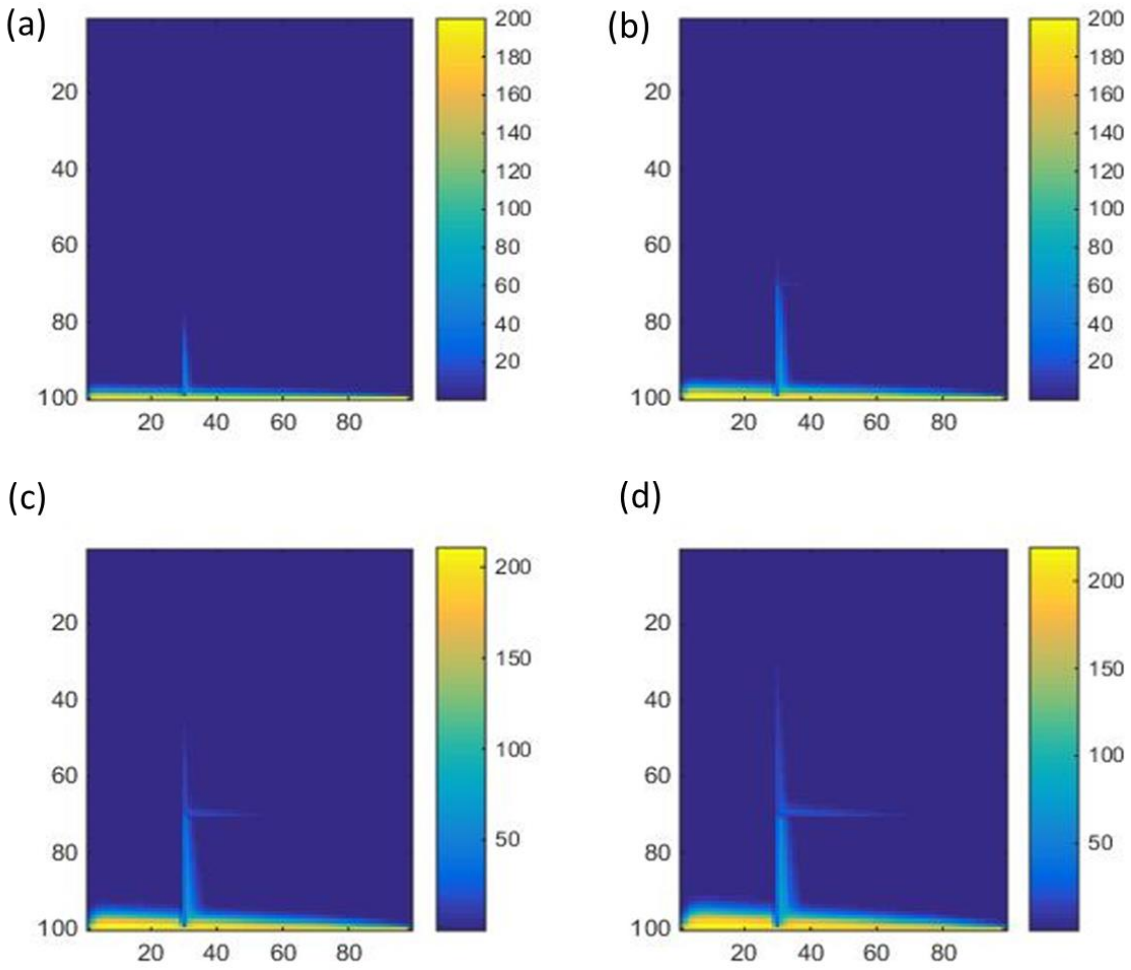

Figure 11. Particle spatial distribution after (a)2h, (b)4h, (c)6h, (d)8h transport for matrix porosity=0.15

CHAPTER IV

NEUTRON POROSITY LOGS SIMULATION RESULTS

4.1 Verification with MCNP Code

As introduced in Chapter 2, simulating Neutron Porosity Logs by solving Neutron Diffusion Equation is a simplified method. In this chapter, we will first verify the accuracy of this method by running a same case published by R. Duenckel, et al. in 2012. In this synthetic case, the formation was assumed to be sandstone with a porosity of 0.283 and a matrix absorption cross-section of 10 c.u.. Formation was saturated with water, whose absorption cross-section was considered to be 22 c.u.. The proppants containing 0.1% by weight of boron carbide had an absorption cross section of 92 c.u.. There was a single fracture with a certain width, placing in the center of the formation. The synthetic formation was vertically 40cm below the source to 100cm above the source. The neutron source strength was 1.5×10^5 neutrons/s. The correlated parameters for this sandstone formation applied in Neutron Diffusion Equation are listed in Table 4, they were correlated by reading Fig.2 and Fig.3. The slowing down length was 12cm as read from Fig.2. The loss in near detector neutron count rate via different weight percent of CB_4 in proppants for different fracture width was calculated and compared with results run by MCNP5 as shown in Fig.12. Noticing that in the original publication, there was no indication of the source and detector distance. We back engineered the parameter by matching the results for 1cm width fracture, and this distance tended to be 20cm in this case. The average difference of the two simulation results for each fracture width was calculated and listed in Table 5. Both MCNP simulation and Neutron Diffusion Equation simulation indicated

the similar increasing trend of neutron count rate lost in the presence of boron carbide, which confirmed the efficiency of boron carbide as contrast agents. That the average difference of the two simulation results for each fracture width was less than 1% further confirmed the accuracy of Neutron Diffusion Equation simulation method as a fast analysis tool.

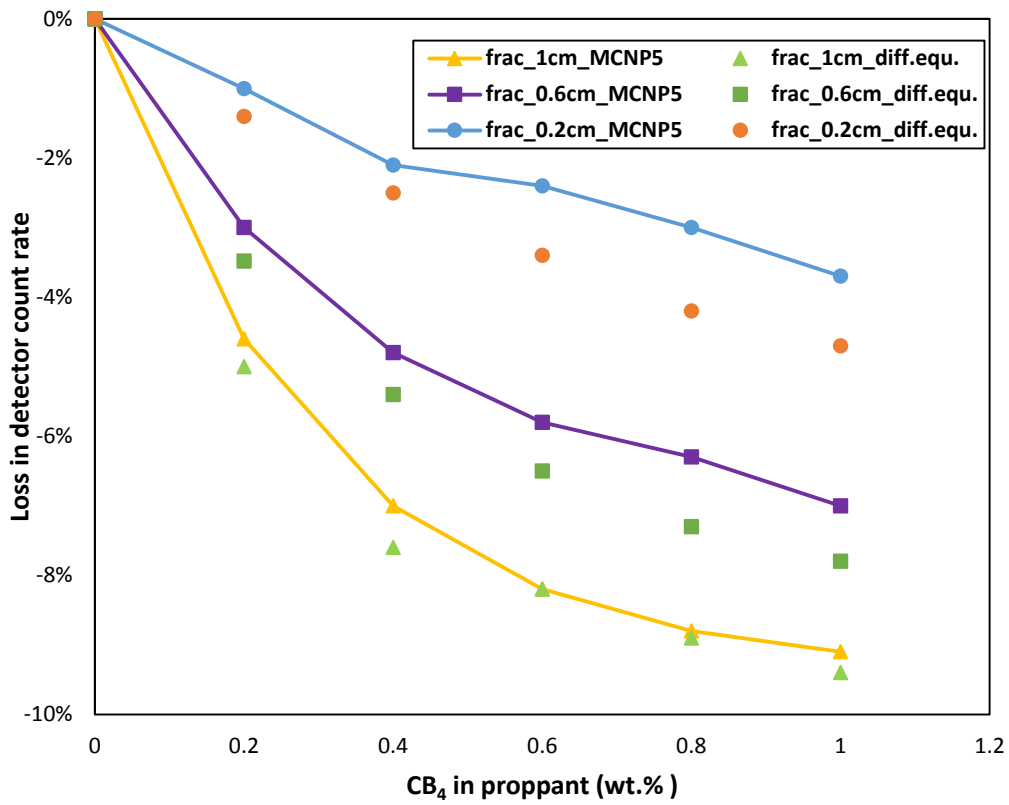

Figure 12 Simulation results comparison of MCNP code (Duenckel et al. 2012) and neutron diffusion equation

Table 4. Macro-parameters for a sandstone formation with a porosity of 0.283 in neutron diffusion equation

D_1	Σ_{r_1}	D_2	Σ_{r_2}
128.16	0.89	0.8	0.0134

Table 5. Average difference and error between MCNP5 simulation results and neutron diffusion equation simulation results for different fracture width.

Fracture Width	1cm	0.6cm	0.2cm
Average Difference	0.3%	0.7%	1%
Average Error	4.3%	13.6%	33.5%

4.2 Single Fracture Sensitivity Analysis

4.2.1 Sensitivity analysis on properties of fractures

The impact of particles concentration on depth-by-depth Neutron Porosity Logs is evaluated by applying Eq. (31). We use the same formation parameters as the verification case mentioned above as shown in Table 4. The formation geometry with the location of fracture is shown in Fig.13. Depth-by-depth neutron logs for different particle concentration is shown in Fig.14. The simulation results indicate that the enhanced neutron porosity logs can precisely locate the fracture. Furthermore, the neutron count rate in the near detector decreases significantly as particle concentration increases.

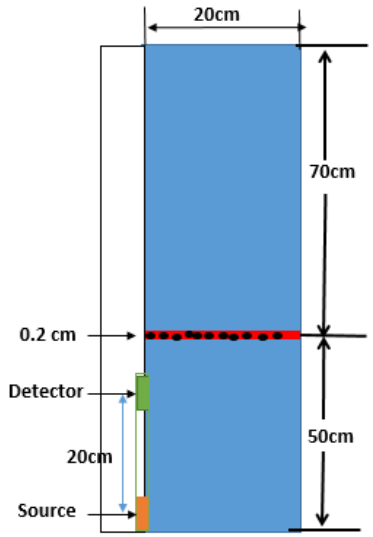

Figure 13. Schematic diagram of Neutron Porosity Log simulation

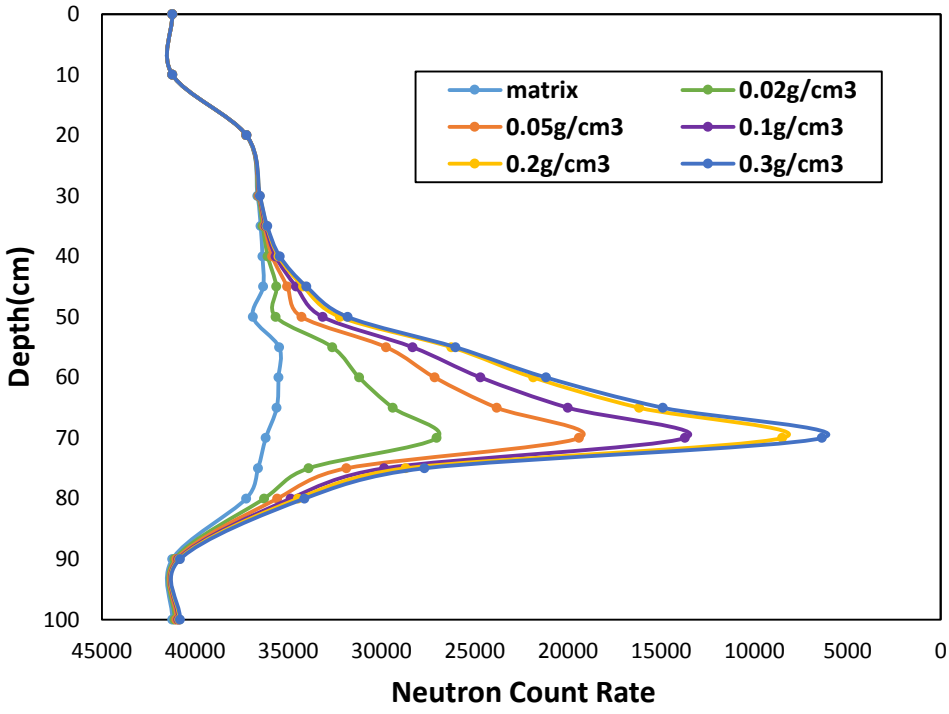

Figure 14. Neutron count rate for different contrast agents concentration (fracture width=0.2cm)

In addition, the impact of fracture width on Neutron Porosity Logs is also evaluated. The results are shown in Fig.15 and Fig. 16. As fracture width decreases, the difference of neutron count rates between fractured and un-fractured formation becomes smaller and smaller. Fig.16 shows the maximum decrease percentage in neutron count rate via different fracture width for different particle concentrations. It can be observed that for different particle concentrations, the minimum detectable single fracture width remains almost the same, which is about 0.0005cm, in micro scale.

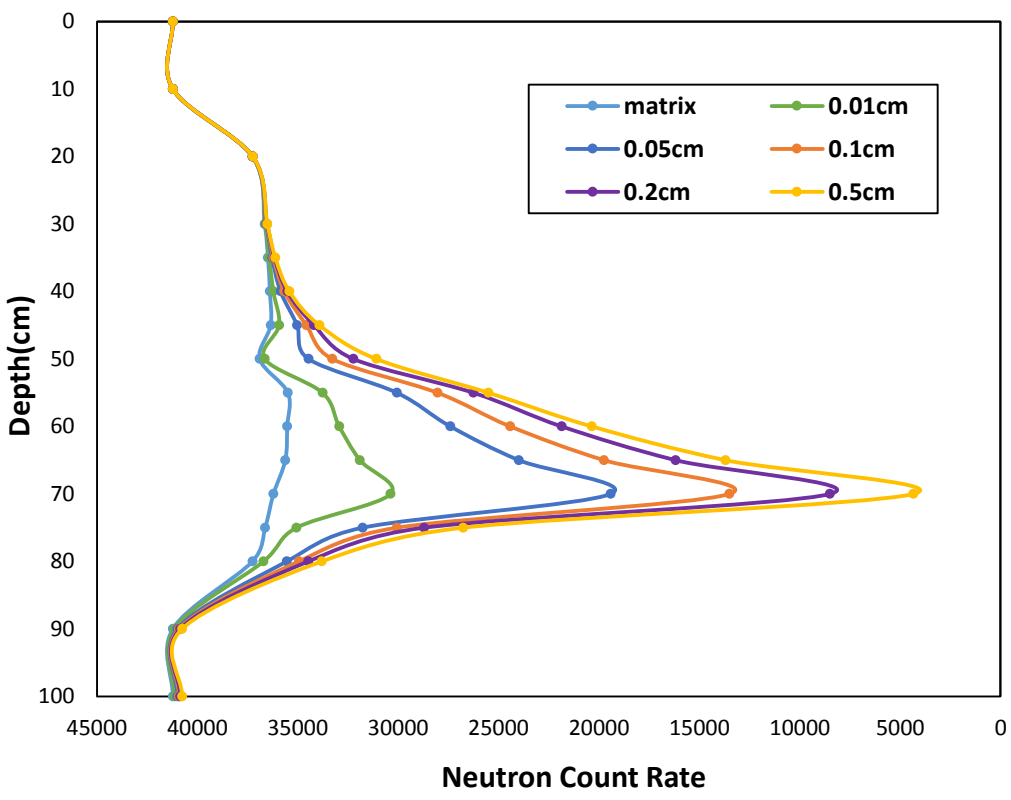

Figure 15. Neutron count rate for different fracture width (contrast agents concentration = 0.2g/cm^3).

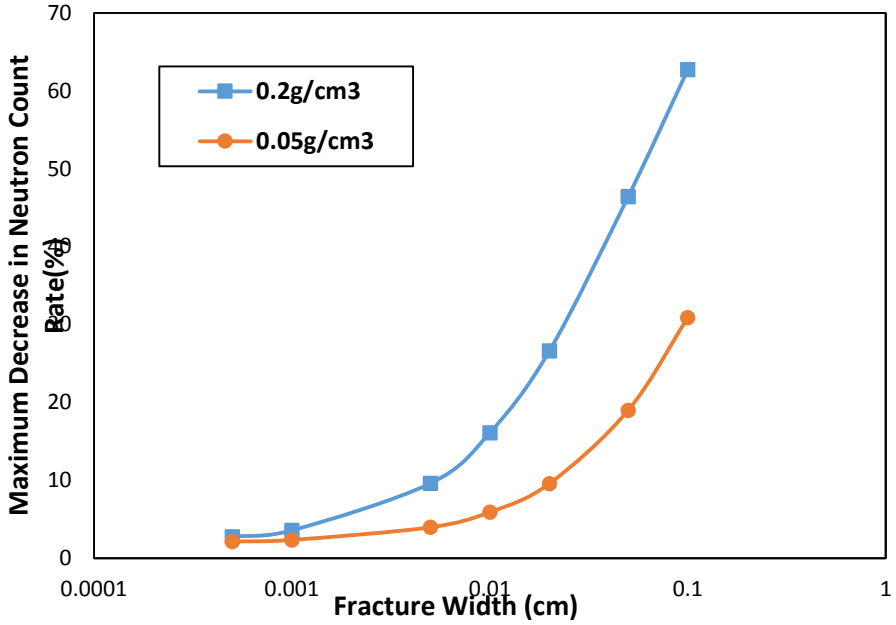

Figure 16. Maximum neutron count rate decrease for different fracture width (contrast agents concentration = 0.2g/cm^3).

4.2.2 Sensitivity analysis on properties of formations

Equations (24) – (29) are applied to calculate how matrix porosity will influence the parameters in Neutron Diffusion Equation. Fig.17 shows the Neutron Porosity Logs for different matrix porosity (the matrix is assumed to be sandstone, and the capture cross section is set as 10c.u.). Though neutron diffusion properties vary sharply in the range of porosity from 0.03 to 0.2 (as shown for diffusion length in Fig.2), it does not quite influence the final neutron porosity logs, as indicated by the simulation results. When porosity as high as 0.4, it will do make the neutron count rates in matrix part decrease a lot. However, in the research scope of the paper, tight reservoir, we can basically consider

that formation porosity has no significant influence on the simulated neutron porosity logs.

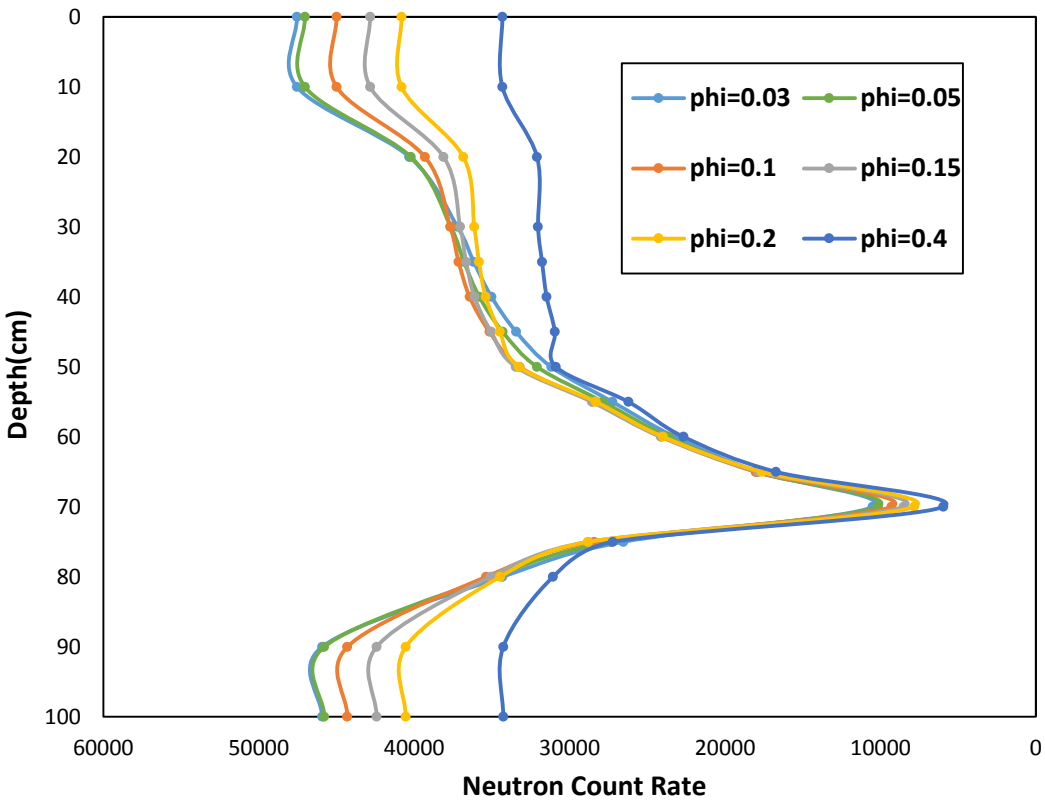

Figure 17. The impact of formation porosity on Neutron Porosity Logs (matrix capture cross section equals to 10 c.u.).

Besides the formation porosity, the capture cross section of matrix will also influence a lot on the final neutron porosity logs. Chloride in formation water will be one of the reasons that cause the capture cross section to be abnormally high. Fig. 18 shows the neutron porosity logs for sandstone matrix with different capture cross section, while the porosity remains same as 0.1. As shown in the simulation results, increasing matrix capture cross section will have a much more significant effect on decreasing the matrix neutron count rate. An increase of capture cross section about 2 c.u. will cause the decrease

of neutron porosity for about 20%. Furthermore, it will also make the peak causing by the presence of the fracture with contrast agents less significant. Thus, we should take serious consideration of the formation lithology and chloride water existence (information that can usually be gained from other logging tools) when applying this technique.

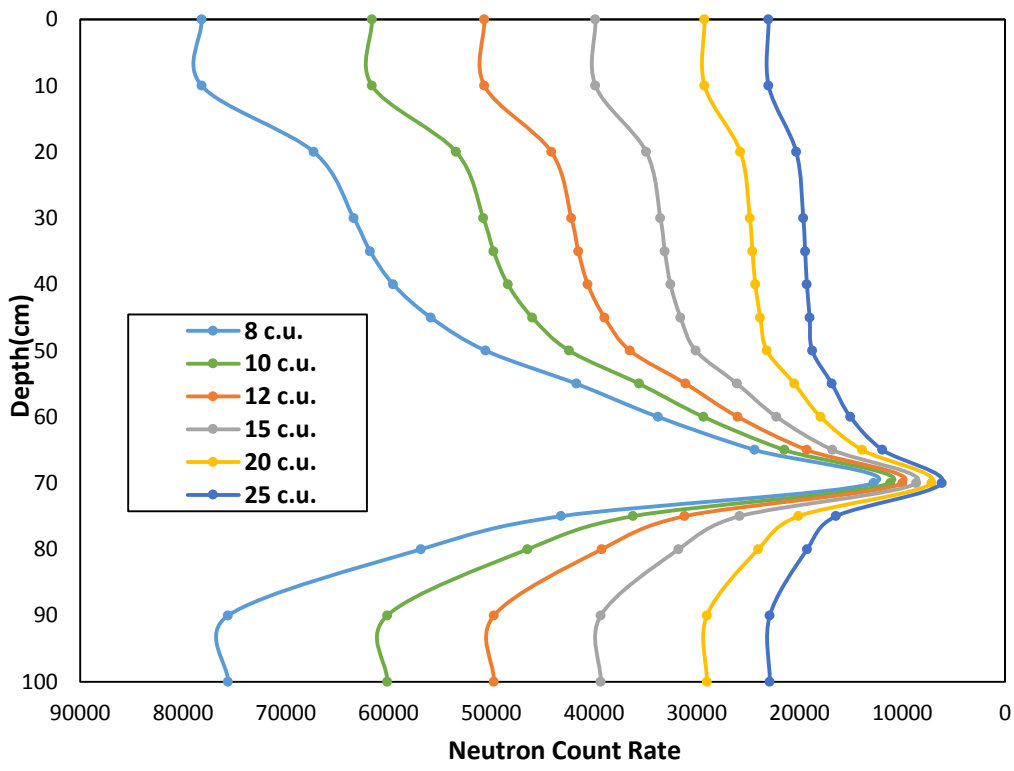

Figure 18. The impact of different matrix capture cross section on Neutron Porosity Logs (matrix porosity =0.1).

Furthermore, Fig.19 shows the simulation results for different formation lithology (constant porosity=0.1, constant capture cross section=10 c.u.). There is no detectable difference in this method for different matrix lithology, as long as the porosity and the

matrix capture cross section are constant. It is also in consistence with the information that Fig.2 and Fig.3 offer us, that is, the lithology of the formation does not influence the neutron diffusion parameters a lot.

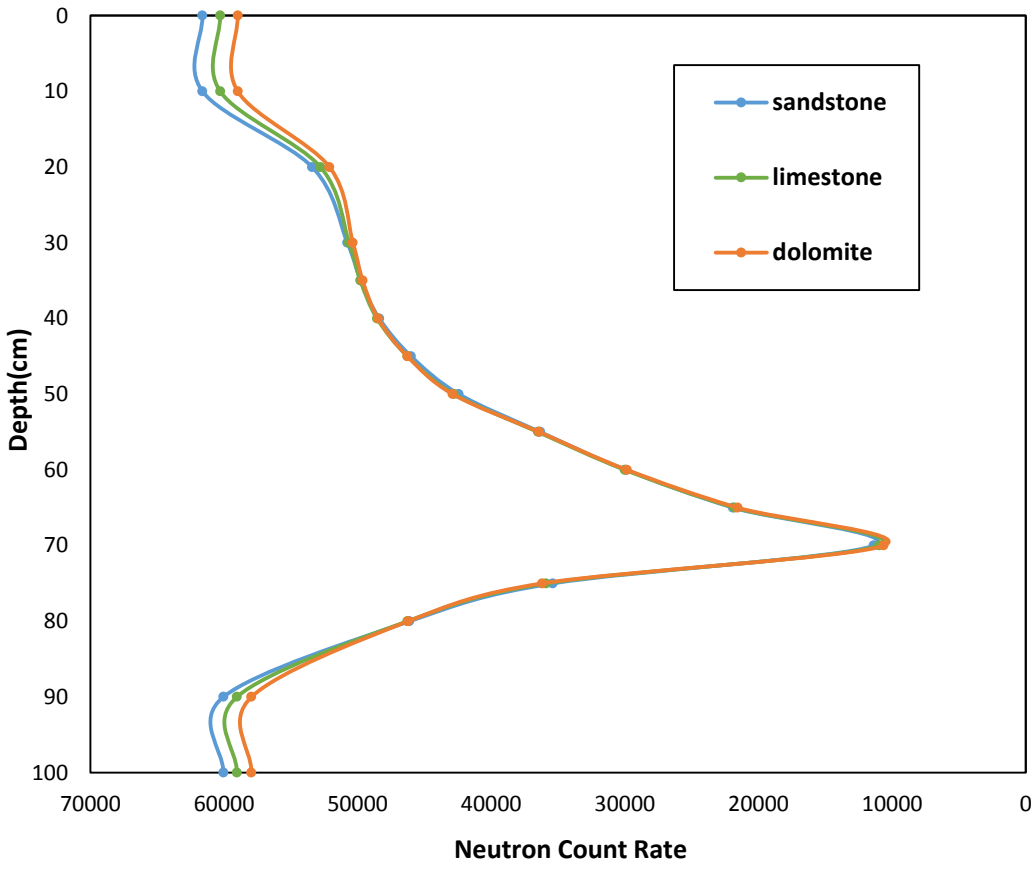

Figure 19. Neutron Porosity Logs for different formation lithology.

4.3 Multi Fractures Characterization

Two parallel fractures with the same constant concentration of contrast agents (0.2 g/cm^3) in it are investigated as shown in Fig.20. The only parameter we change is the

distance between the two parallel fractures, the simulation results are shown in Fig.21 and Fig.22.For fracture distance from 2cm-6cm, the peak of simulated neutron porosity logs becomes wider and wider, as shown in Fig.21. For fracture distance as large as 8cm, the peak begins to separate. And then, as the fracture distance continues to increase, the distance between separate peaks also becomes larger and larger as shown in Fig.22. Thus, the technique is available in distinguishing and locating different perforation zones.

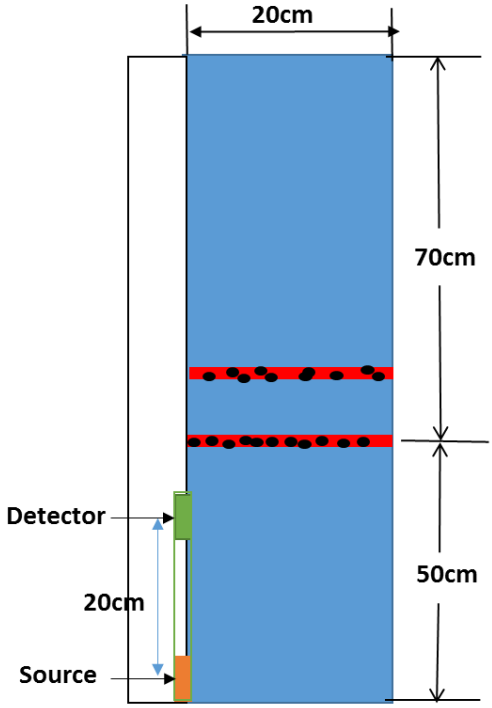

Figure 20. Schematic Diagram of two parallel fractures simulation.

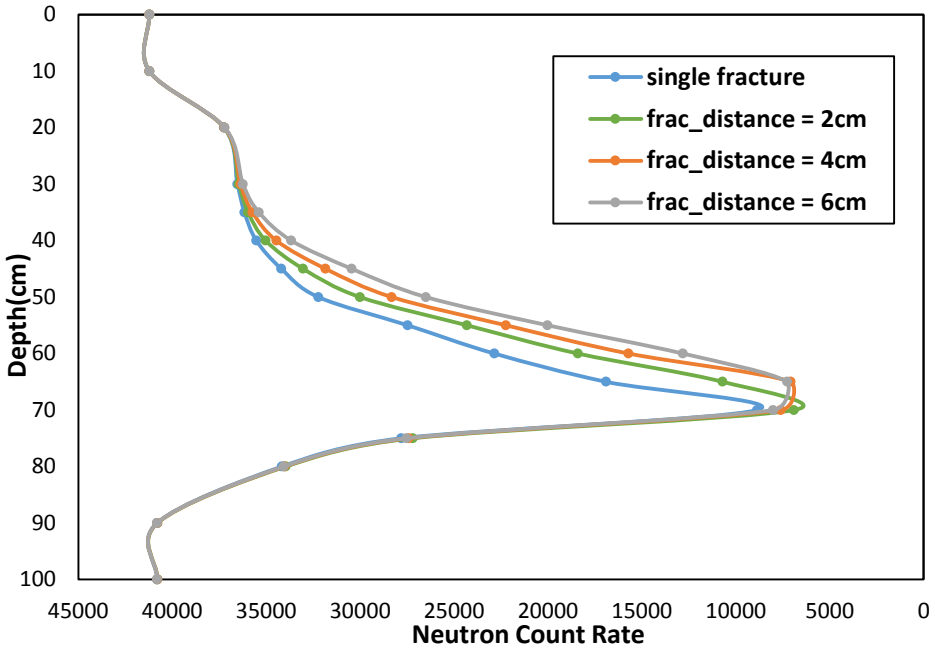

Figure 21.Neutron Porosity Logs for different fracture distance (2cm-6cm).

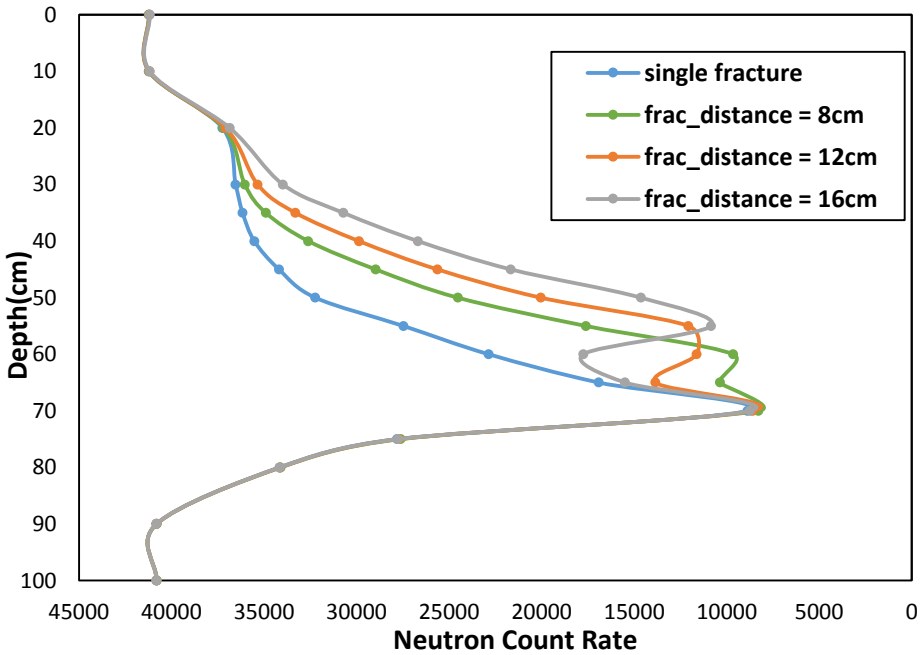

Figure 22. Neutron Porosity Logs for different fracture distance (8cm-16cm).

CHAPTER V

SYNTHETIC CASES FOR FRACTURE CHARACTERIZATION

5.1 Introduction

In this chapter, the electrically transport simulation and the neutron porosity logs simulation will be combined. The overall simulation process is as following: 1) estimate the electric field distribution through the location of high electric potential and boundary conditions, 2) simulate the particles spatial distribution under electric field for different transport time, 3) based on the particles spatial distribution, simulate the relative neutron porosity logs for different transport time. The spatial distribution of high neutron absorbing particles (eg. boron carbide) will influence the neutron capture cross section in fractures and the adjacent matrix (considering leakage), and thus influence the neutron porosity logs.

5.2 Evenly Spaced Fractures Characterization

We first investigate how the evenly spaced fractures and the spacing among them will influence the neutron porosity logs. In Table.6, we calculate the maximum decrease of neutron count rate (the decrease of peak) for different fractures spacing and different transport time. When the fracture spacing decreases from 15cm to 2.5cm (it is a dramatically change in the sense of fracture density), the decrease of the neutron porosity logs is only about 6% percent for all the transport time. Thus, other data analyzing methods, like calculated the relative change needed to be introduced to differentiate formations with different fracture densities, which will be shown in part 5.3

Table 6. Maximum neutron count rate decrease in the detector, for different fracture spacing formations and for different transport time.

Maximum count rate decrease	2.5cm	7.5cm	15cm
2h	53.5%	50.2%	48.5%
4h	55.3%	51.8%	49.6%
6h	56.0%	52.7%	50.2%
8h	56.3%	53.2%	50.6%

A synthetic formation with 15cm spacing fractures on the up-half part, 2.5cm spacing fractures on the down-half part, and two orthogonal fractures functioning as the source of contrast agent particles is generated. An electric field with a strength of about 100v/m in x and y direction is applied. The particles spatial distribution for 2h, 4, h, and 8h transport time is shown in Fig.23. Basically, particles will transport in the direction of decreasing electric potential, and the sharper the electric potential decreases, the faster the particles transport will be. Fig.24. shows the neutron porosity logs for the different particles spatial distribution relating with the different transport time. From the neutron porosity logs, we can figure out that the upward part of the formation is with a lower fracture density, while the downward part of the formation is with a higher fracture density. However, the neutron porosity does not change a lot for different transport time.

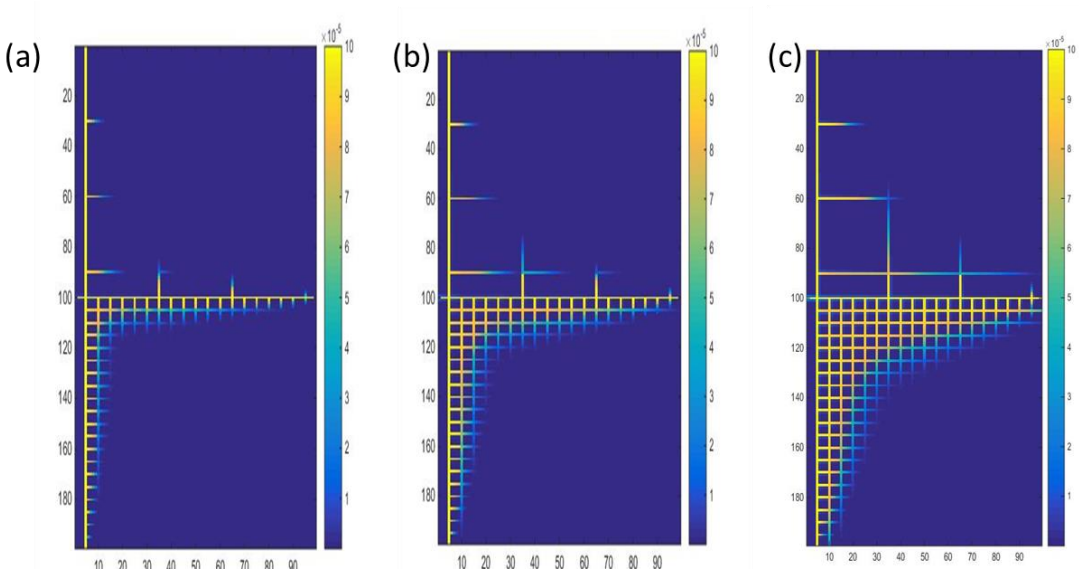

Figure 23. Synthetic formation with evenly spaced fractures: particles spatial distribution after applying electric field for (a) 2h, (b) 4h, (c) 8h.

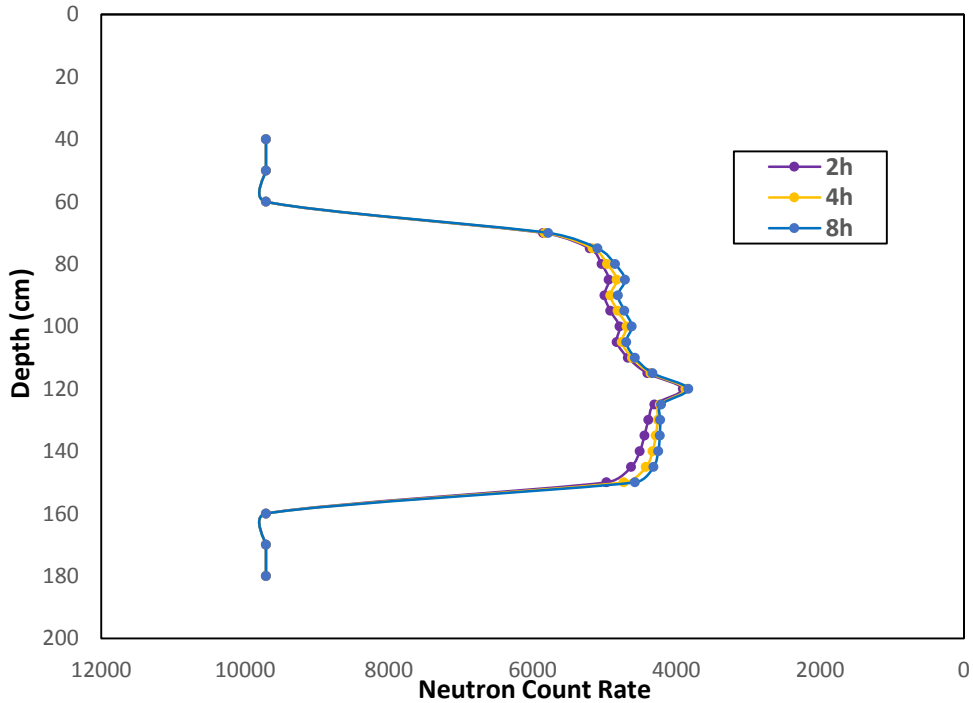

Figure 24.Synthetic formation with evenly spaced fractures: neutron porosity logs after applying electric field for (a) 2h, (b) 4h, (c) 8h.

5.3 Formations with Different Secondary Fracture Densities

The synthetic 2D case is modeled as a tight formation with matrix porosity of 0.03 (another case with a matrix porosity of 0.1 will show later) and a matrix capture cross section of 10 capture unit. As shown in the left part of Fig.25, there is a 0.5cm-width and 20cm-length hydraulic fracture functioned as the source of particles. It is assumed to maintain a constant particle concentration of $0.2 g/cm^3$. And the particle zeta potential is assumed to be 100MV. The secondary fracture densities in the four synthetic cases are 1%, 2%, 4% and 8% respectively. Their detailed geometry is shown in the right part of Fig.25. Here, the fracture density is defined as the volume of fractures dividing the volume of simulated formation.

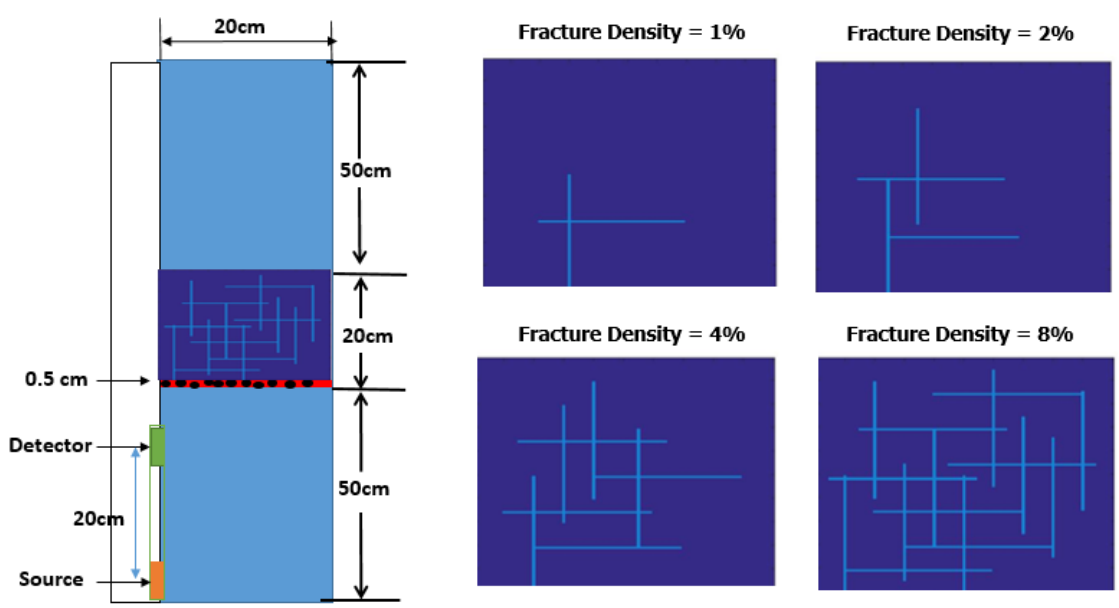

Figure 25. Synthetic formation with different natural/induced fracture density of 1%, 2%, 4% and 8%.

We apply a 30V electric potential at the perforation point of hydraulic fracture, and then assume the electric potential of far boundary in x and y direction of the fractured formation to be 0V. Thus the relative electric field strength in x and y direction will both be about 150V/m. An estimation of the electric field distribution is shown in Fig.26.

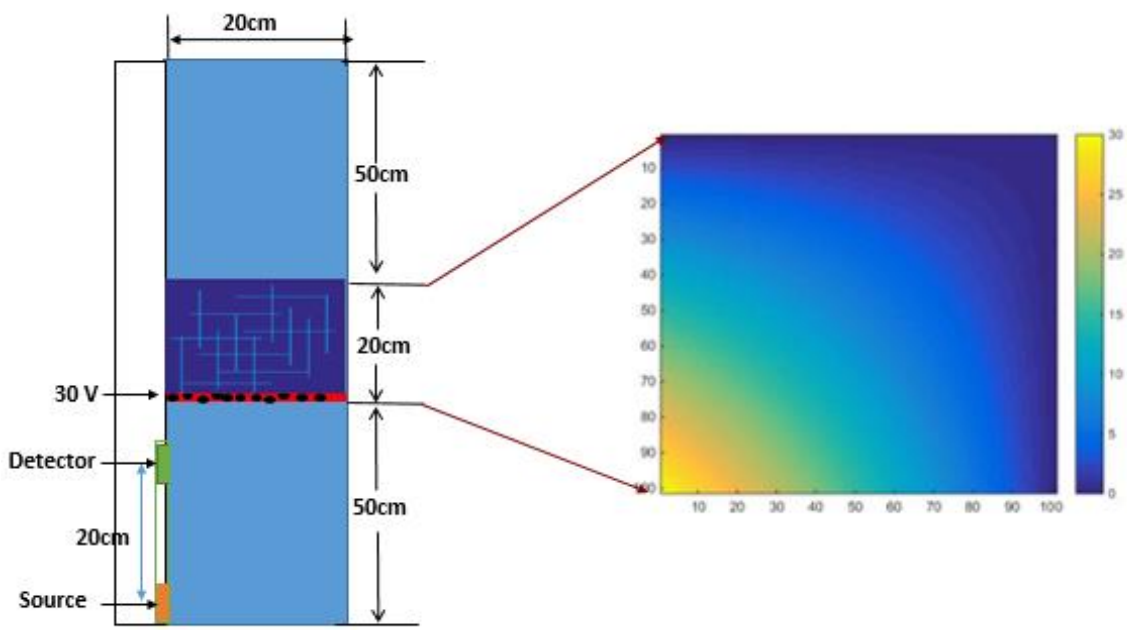

Figure 26. Electric field distribution of the synthetic formation.

With electric field being applied, charged contrast agents will transport from hydraulic fracture to secondary fractures. The contrast agents spatial distribution via time for different fracture density is shown in Fig. 27. Noticing that the end point of the fractures whose concentration exceeds 0.2 g/cm^3 is set to be 0.2 g/cm^3 only for plotting purpose. The simulation results confirmed that the external electric field can significantly

enhance the transport of particles to secondary fractures, while no significant leakage to formation at the same time.

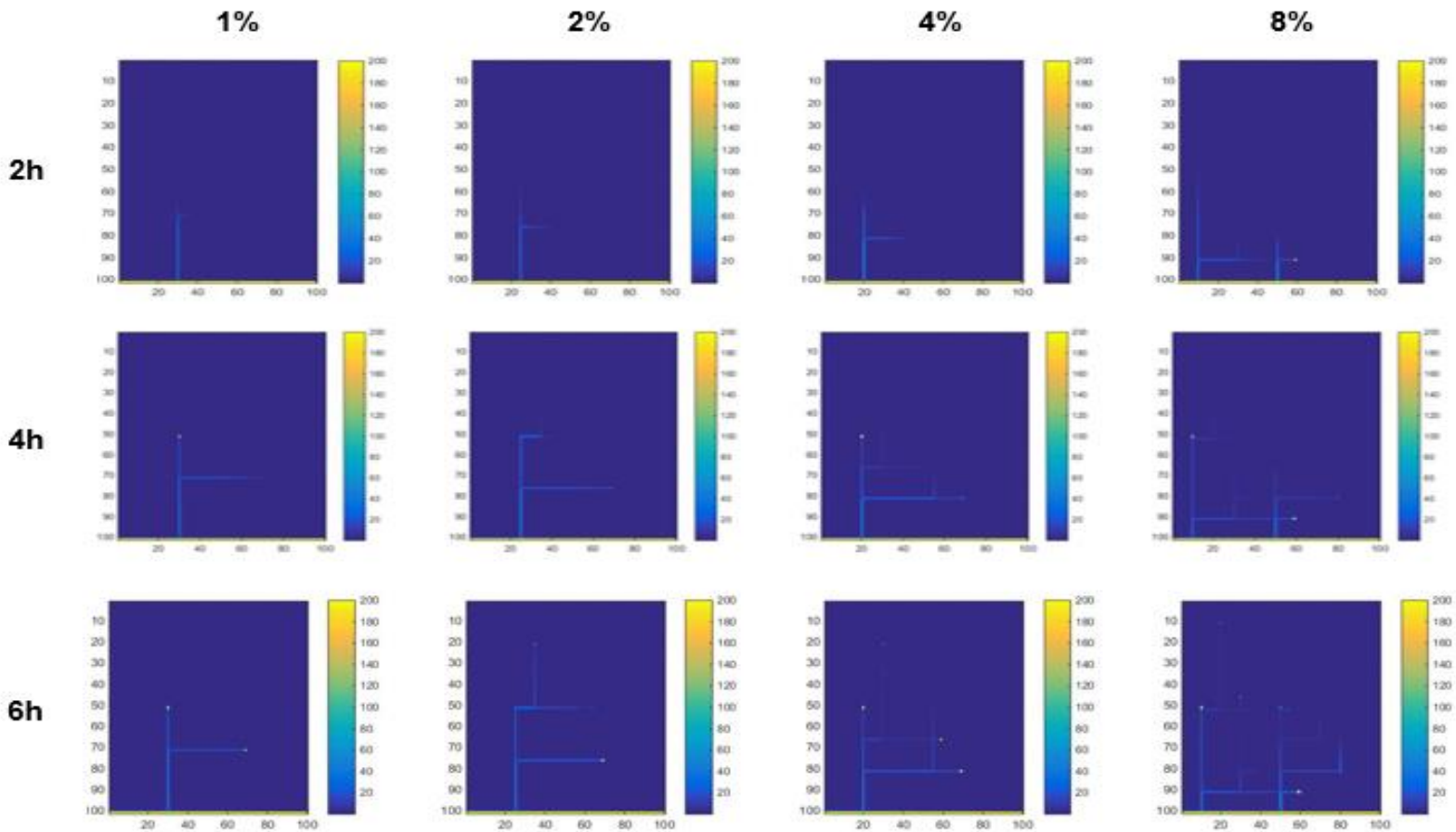

Figure 27. Particle spatial distribution after applying electric field for 2h, 4h, and 6h. Formations with fracture density of 1%, 2%, 4% and 8% are compared (matrix porosity = 0.03, the concentration scale is in kg/m^3).

The simulated neutron porosity logs for different transport time are shown in Fig.28. Formations with different fracture densities are also compared for each time. As discussed in 5.3, the difference in neutron count rates of formations with different fracture densities is hardly detected. Thus, relative change of simulated neutron porosity (Φ_N) via depth before and after applying electric potential field for different time is calculated and compared in Fig.29. The relative change of neutron porosity becomes larger as transport time increases. The maxim relative change is up to 30% for the formation with 8% fracture density and a transport time of 6h. The first four hours are a best time to differentiate different density formation in this case. The difference of relative change for neutron porosity for low fracture density formations (1% and 2%) becomes less and less detectable as transport time increases (as shown in 6h case).

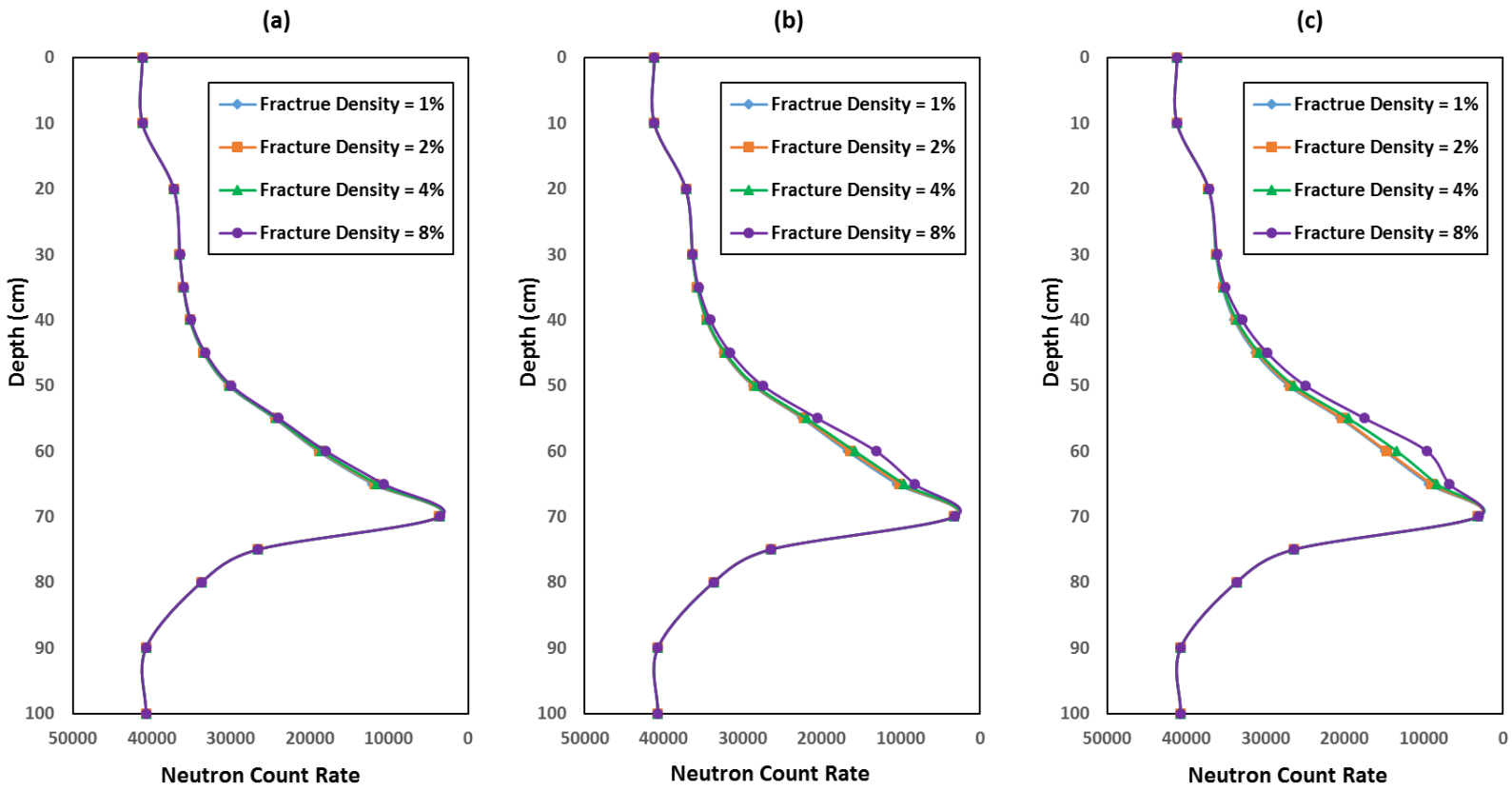

Figure 28. Neutron Porosity Logs after applying electric field for (a) 2h, (b) 4h, and (c) 6h, formations with different fracture densities are compared (matrix porosity = 0.03).

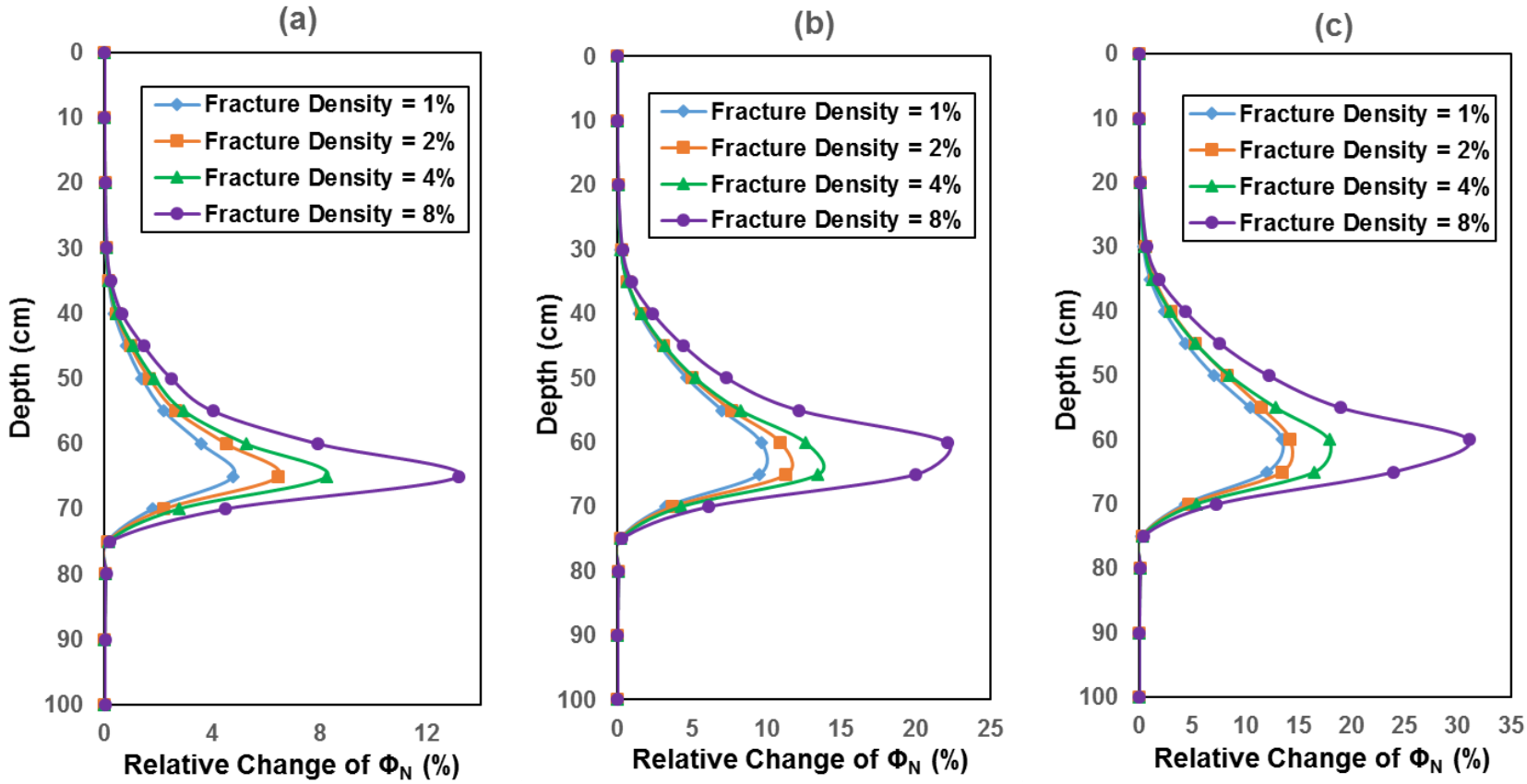

Figure 29. Relative change of Φ_N before and after applying electric field for (a) 2h, (b) 4h, and (c) 6h, formations with different fracture densities are compared (matrix porosity = 0.03).

It is worthwhile to mention that during the whole transport period, formation with 8% fracture density remains a much higher relative change of neutron porosity than any other formations. It is because in this synthetic case, formation with 8% fracture density is the only formation that secondary fractures have two connection points with hydraulic fractures. As Fig.30 indicates, it will make the total particles amount in formation with 8% fracture density much higher than that of other formations. And the assumption that formation with a higher secondary fracture density has more chance to interact with hydraulic fracture is also really sound. Thus, it is reasonable for us to conclude that the proposed technique will be of high sensitivity in detecting high induced/natural fracture density zones.

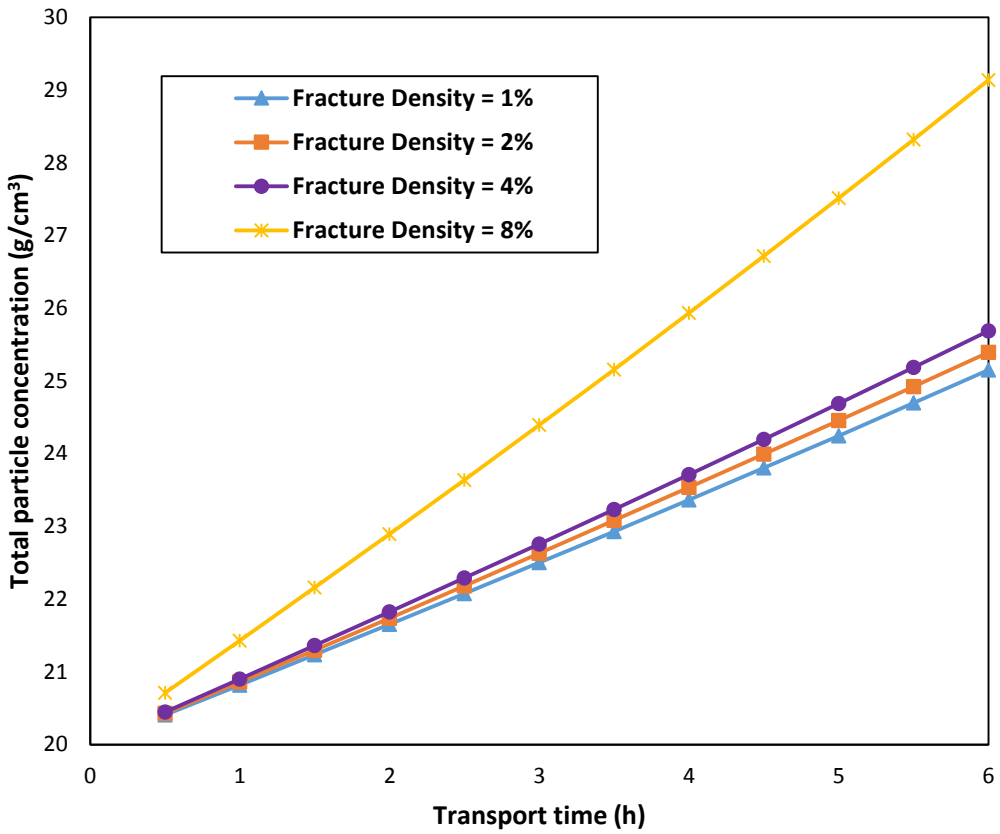

Figure 30. Total particle concentration in formation via transport time for formations with different fracture density

As investigated in 2.2, particles will leak into the matrix as matrix porosity increases. Thus, we set the matrix porosity to be 0.1, and keep other parameters just as the same, rerunning the case. The new particles spatial distribution for different transport time and for formations with different fracture density is shown in Fig.31. Comparing Fig.31 with Fig.27, we can find a little bit leakage of particles into the matrix adjacent to the fractures. However, the Neutron Porosity Logs do not have detectable changes when matrix porosity changes (as compared by Fig.32 and Fig.28).

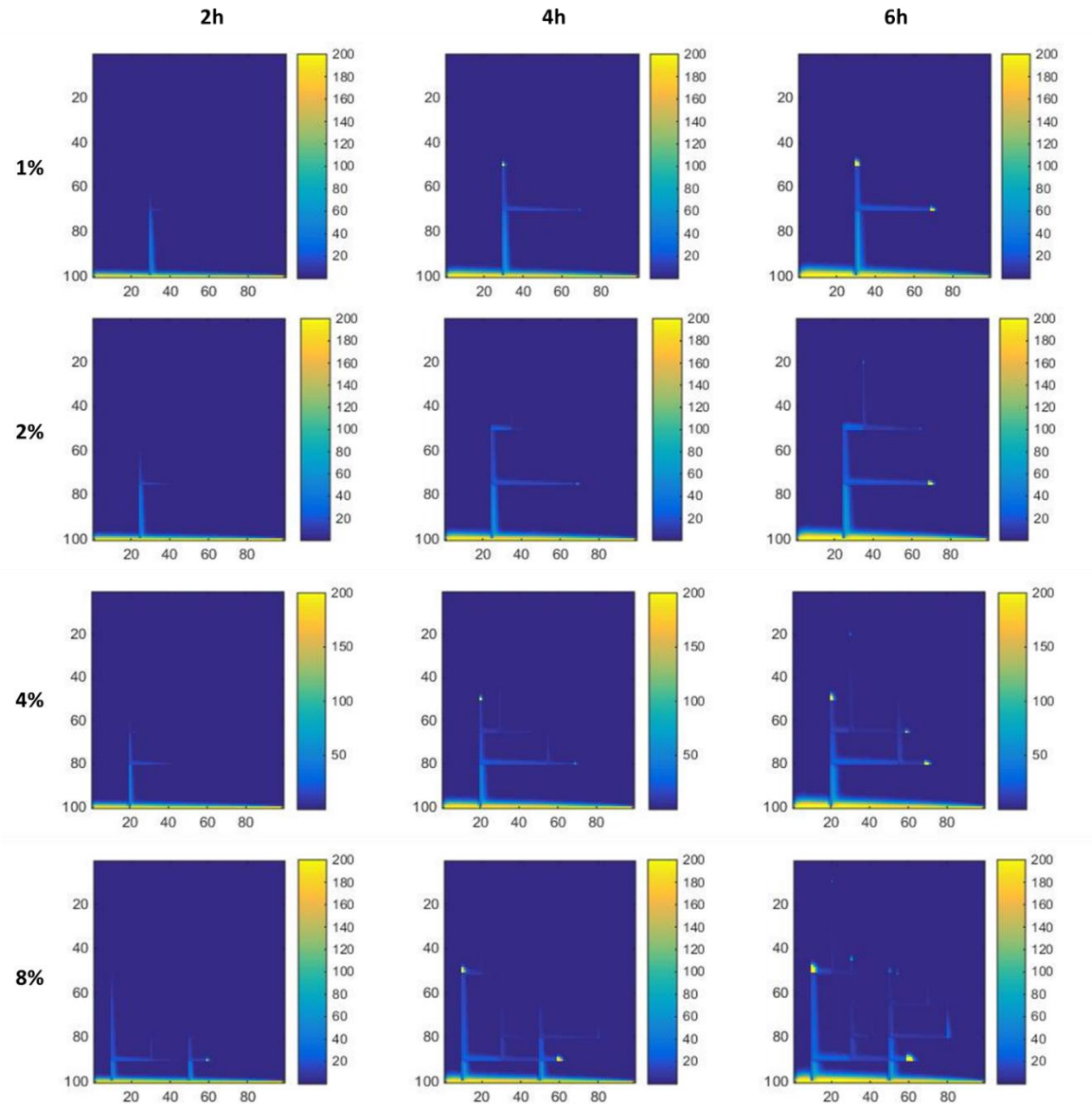

Figure 31. Particle spatial distribution after applying electric field for 2h, 4h, and 6h. Formations with fracture density of 1%, 2%, 4% and 8% are compared (matrix porosity = 0.1, the concentration is in kg/m3).

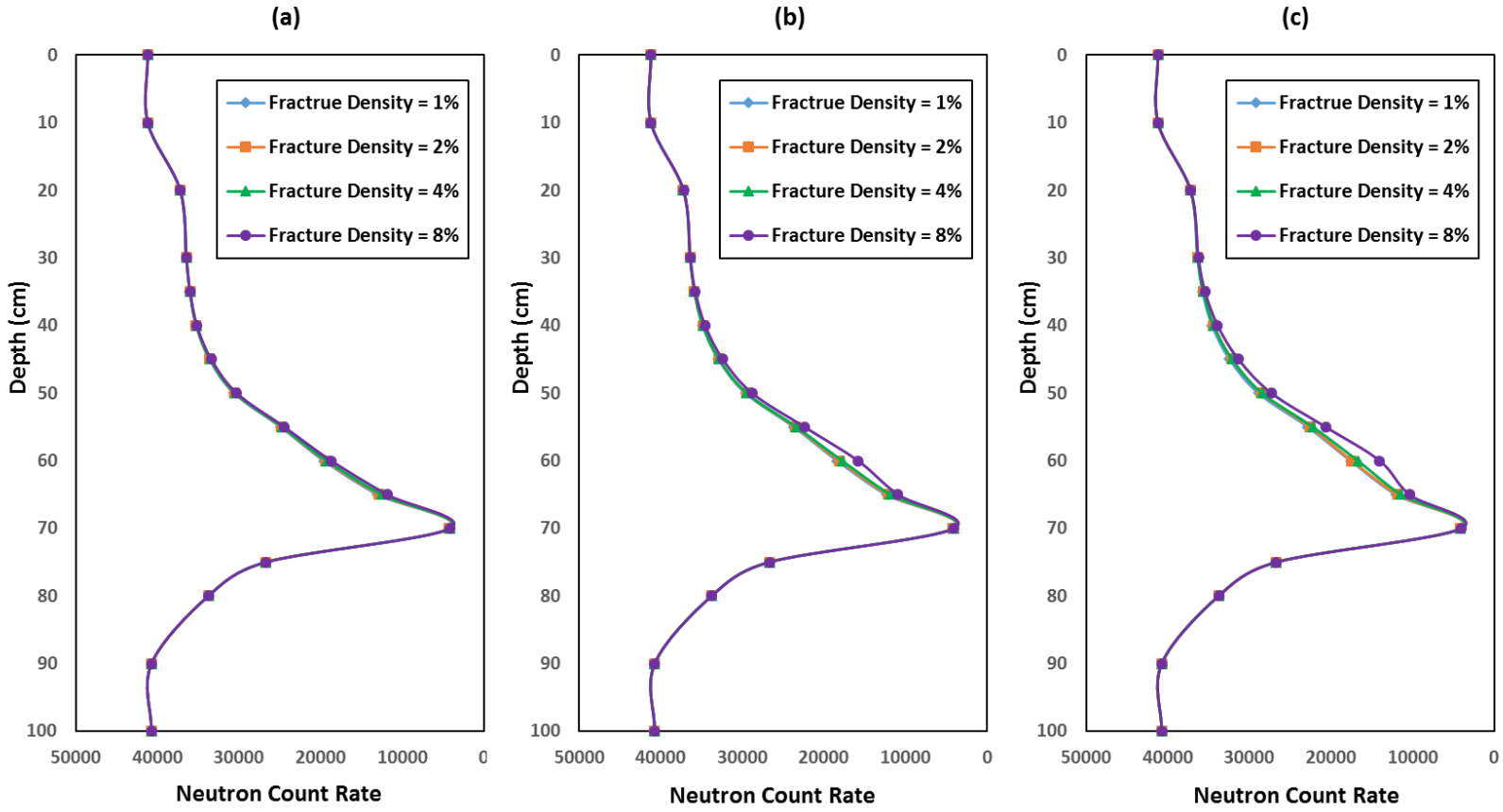

Figure 32.Neutron Porosity Logs after applying electric field for (a) 2h, (b) 4h, and (c) 6h, formations with different fracture densities are compared (matrix porosity = 0.1).

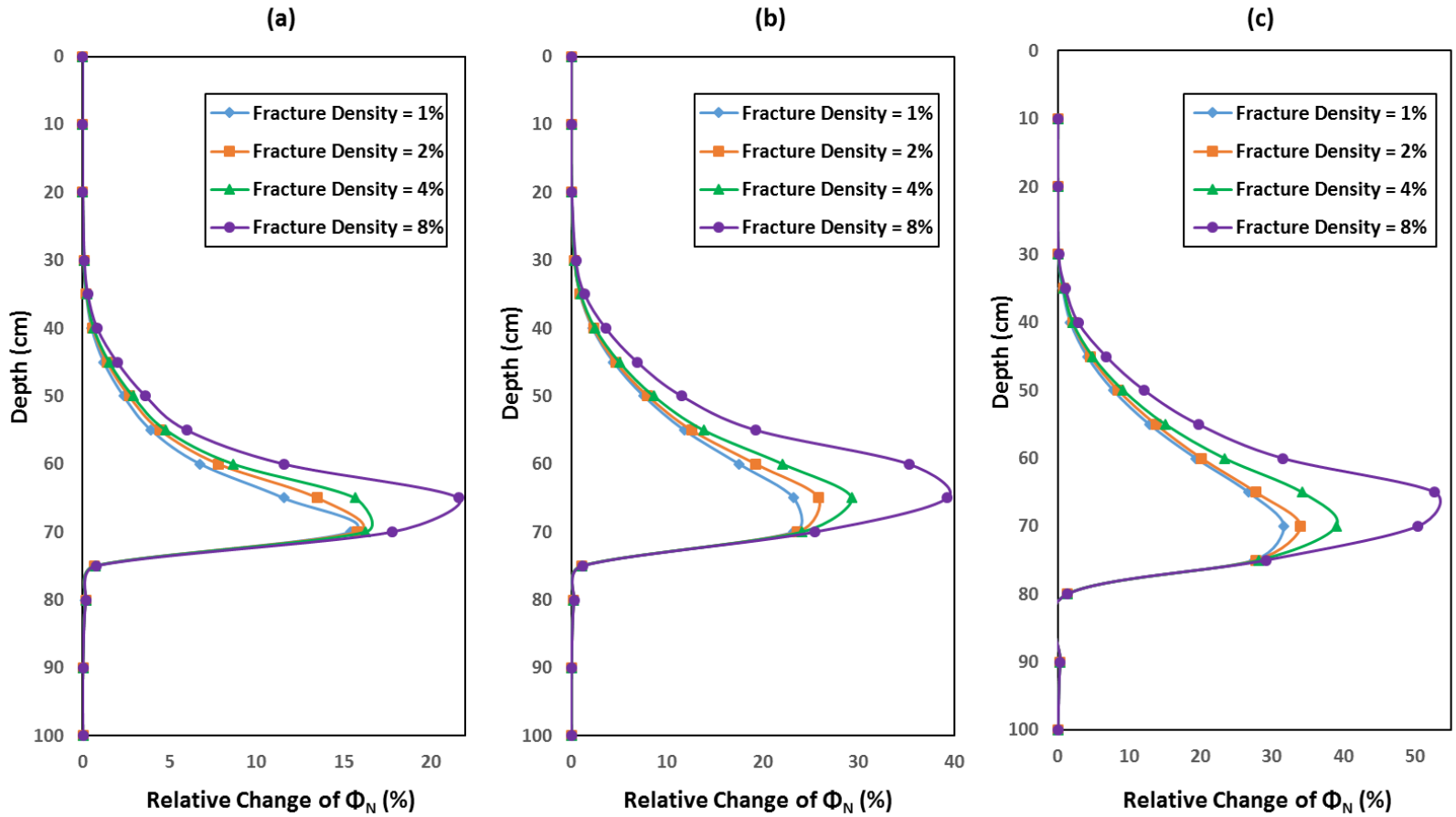

Figure 33. Relative Change of Φ_N before and after applying electric field for (a) 2h, (b) 4h, and (c) 6h, formations with different fracture densities are compared (matrix porosity = 0.1)

Fig.33 shows the relative change of neutron porosity logs before and after applying electric field for different time for matrix porosity equals to 0.1. Comparing with Fig.29, the log is no longer perfectly discretized for 2h transport time, because of the leakage from hydraulic fracture to matrix. Furthermore, the relative change of neutron porosity is up to 50% percent for formation with a density of 8%, a lot higher than porosity equaling to 0.1 case. In this case 4h might be a good time to distinguish formation with different fracture density. For all the transport time, formation with a fracture density of 8% remains a much higher relative change compared to others, which confirms the aforementioned conclusion that the proposed technique is of high resolution in detecting formations with high fracture density.

CHAPTER VI

CONCLUSIONS

The previous applications of boron carbide to enhance the sensitivity of neutron logs are all focused on locating the proppants. In this paper, for the first time we (a) enhanced the mobility and propagation of these contrast agents into secondary fracture network using an externally applied electric field and (b) characterized the fracture density in un-propped area using the enhanced neutron porosity logs. Based on the numerical simulation of the whole procedure, we gain the following conclusions:

(1) External electric field can significantly enhance the transport of particles into secondary fractures.

(2) The electrically transport will be mainly influenced by particles zeta potential and electric field strength. To transport a same distance, increasing particles zeta potential and electric field strength can both decrease the transport time.

(3) Increasing particle zeta potential has a more significant effect on accelerating the transport than increasing electric field strength for the same amount

(4) There will be no significant leakage of particles into the matrix if the matrix porosity is small (tight reservoir, porosity < 0.1). However, as the matrix porosity becomes larger and larger, the leakage will become much more significant.

(5) Solving neutron diffusion equation is a fast way to simulate neutron porosity logs, while maintaining an acceptable accuracy comparing to the results solved by MCNP code.

(6) The presence of contrast agents in a single hydraulic fracture will lead to a sharp decreasing peak on the neutron porosity logs, and the peak can well indicate the location of the fracture.

(7) The relative change of the simulated neutron porosity will increase as contrast agents concentration increases, and as the width of hydraulic fracture increases.

(8) The minimum detectable fracture width is about 0.001cm, which does not influence much by the concentration of contrast agents in the fracture.

(9) The porosity of the formation will influence the simulated neutron porosity, but the influence is not significant within a low porosity range.

(10) The capture cross section of the formation will have a significant influence on neutron porosity logs. This technique is not applicable for formation with high neutron capture cross section (>25 c.u.).

(11) Different formation lithology with same porosity and capture cross section will make no detectable difference in this technique.

(12) Two hydraulic fractures in the presence of contrast agents can be detected as two separate peaks on the neutron porosity logs if the distance between them is large enough (8cm in the simulated case). The distance between them can be indicated by the width of the single peak or the distance between the two peaks.

(13) Formations with different fracture density is distinguishable through the proposed technique by calculating the relative of the neutron porosity logs. The relative change is up to 30% for the formation with 8% fracture density, and it will be higher if the matrix porosity increases.

(14) The proposed technique is of high resolution in locating high fracture density part of the formation.

REFERENCES

Allen, L., Tittle, C., Mills, W. et al. 1967. Dual-Spaced Neutron Logging for Porosity. *Geophysics* **32** (1): 60-68.

An, C., Alfi, M., Yan, B. et al. 2016. A New Study of Magnetic Nanoparticle Transport and Quantifying Magnetization Analysis in Fractured Shale Reservoir Using Numerical Modeling. *Journal of Natural Gas Science and Engineering* **28**: 502-521.

Chi, L., Elliott, M., Heidari, Z. et al. 2014. Assessment of Micro-Fracture Density Using Combined Interpretation of Nmr Relaxometry and Electromagnetic Logs. Presented at Unconventional Resources Technology Conference (URTEC), Denver, Colorado, USA, 25-27 August. SPE-1922804-MS. http://dx.doi.org/10.15530/urtec-2014-1922804

Dahi Taleghani, A., Ahmadi, M., and Olson, J. 2013. Secondary Fractures and Their Potential Impacts on Hydraulic Fractures Efficiency. Presented at ISRM International Conference for Effective and Sustainable Hydraulic Fracturing, Brisbane, Australia, 20-22 May. ISRM-ICHF-2013-043

Duenckel, R., Smith Jr, H.D., and Smith, M.P. 2012. *Methods of Identifying High Neutron Capture Cross Section Doped Proppant in Induced Subterranean Formation Fractures*. US 8214151 B2.

Ellis, D., Flaum, C., Galford, J. et al. 1987. The Effect of Formation Absorption on the Thermal Neutron Porosity Measurement. Presented at SPE Annual Technical Conference and Exhibition, Dallas, Texas, USA, 27-30 September. SPE-16814-MS. http://dx.doi.org/10.2118/16814-MS.

Ellis, D.V. and Singer, J.M. 2007. *Well Logging for Earth Scientists*: first edition, Springer Science & Business Media. Original edition.

Fang, C., Tong, N., and Lin, J. 1991. Removal of Emulsified Crude Oil from Produced Water by Electrophoresis. Presented at SPE International Symposium on Oilfield Chemistr, Anaheim, California, USA, 20-22 February. SPE-21047-MS.

Gadekea, L., Gartner, M., Sharbak, D. et al. 1991. The Interpretation of Radioactive-Tracer Logs Using Gamma-Ray Spectroscopy Measurements. *The Log Analyst* **32** (01).

Henry, D. 1931. The Cataphoresis of Suspended Particles. Part I. The Equation of Cataphoresis. *Proceedings of the Royal Society of London A: Mathematical, Physical and Engineering Sciences*, **133** (821): 106-129..

Henry, D. 1948. The Electrophoresis of Suspended Particles. IV. The Surface Conductivity Effect. *Transactions of the Faraday Society* **44**: 1021-1026.

Hill, R.J. 2007. Electric-field-enhanced Transport in Polyacrylamide Hydrogel Nanocomposites. *Journal of Colloid and Interface Science* **316** (2): 635-644.

Hunt, L., Reynolds, S., Brown, T. et al. 2010. Quantitative Estimate of Fracture Density Variations in the Nordegg with Azimuthal Avo and Curvature: A Case Study. *The Leading Edge* **29** (9): 1122-1137.

Huotari, H., Trägårdh, G., and Huisman, I. 1999. Crossflow Membrane Filtration Enhanced by an External Dc Electric Field: A Review. *Chemical Engineering Research and Design* **77** (5): 461-468.

Lee, S. 1990. *Oil Shale Technology*: CRC Press. Original Edition. ISBN 0849346150.

Leroy, P., Tournassat, C., and Bizi, M. 2011. Influence of Surface Conductivity on the Apparent Zeta Potential of TiO_2 Nanoparticles. *Journal of Colloid and Interface Science* **356** (2): 442-453.

Luffel, D. and Howard, W. 1988. Reliability of Laboratory Measurement of Porosity in Tight Gas Sands. *SPE Formation Evaluation* **3** (04): 705-710.

Martinez, L.P., Hughes, R.G., and Wiggins, M.L. 2002. Identification and Characterization of Naturally Fractured Reservoirs Using Conventional Well Logs. *The University of Oklahoma, 23p*.

Mulkern, M.E., Masnyk, B., Kramer, H. et al. 2010. A Green Alternative for Determination of Frac Height and Proppant Distribution. Presented at SPE Eastern Regional Meeting, Morgantown, West Virginia, USA, 13-15 October. SPE-138500-MS. http://dx.doi.org/10.2118/138500-MS.

Plegue, T., Frank, S.G., Fruman, D. et al. 1986. Viscosity and Colloidal Properties of Concentrated Crude Oil-in-Water Emulsions. *Journal of Colloid and Interface Science* **114** (1): 88-105.

Randolph, P., Soeder, D., and Chowdiah, P. 1984. Porosity and Permeability of Tight Sands. Presented at SPE Unconventional Gas Recovery Symposium, Pittsburgh, Pennsylvania, 13-15 May. SPE-12836-MS.

Saldungaray, P., Palisch, T., and Duenckel, R. 2012. Novel Traceable Proppant Enables Propped Frac Height Measurement While Reducing the Environmental Impact. Presented at SPE/EAGE European Unconventional Resources Conference &

Exhibition-From Potential to Production, Vienna, Austria, 20-22 March. SPE-151696-MS. http://dx.doi.org/10.2118/151696-MS.

Sharma, M. and Manchanda, R. 2015. The Role of Induced Un-Propped (Iu) Fractures in Unconventional Oil and Gas Wells. Presented at SPE Annual Technical Conference and Exhibition, Houston, Texas, USA, 28-30 September. SPE-174946-MS. http://dx.doi.org/10.2118/174946-MS.

Smoluchowski, M. 1924. Contribution À La Théorie De L'endosmose Électrique Et De Quelques Phénomènes Corrélatifs. *Pisma Mariana Smoluchowskiego* **1** (1): 403-420.

Trusdell, A. and Jones, B.F. 1973. Wateq: A Computer Program for Calculating Chemical Equilibria of Natural Waters. *Journal of Research of the US Geological Survey* **2**(2):233-248

Wright, C., Davis, E., Golich, G. et al. 1998. Downhole Tiltmeter Fracture Mapping: Finally Measuring Hydraulic Fracture Dimensions. Presented at SPE Western Regional Meeting, Bakersfield, California, 10-13 May. SPE-46194-MS. http://dx.doi.org/10.2118/46194-MS.